Chapter 7

Wavelet–Neural–Network Control for Maximization of Energy Capture in Grid Connected Variable Speed Wind Driven Self-Excited Induction Generator System

Fayez F. M. El-Sousy and Awad Kh. Al-Asmari

Additional information is available at the end of the chapter

http://dx.doi.org/10.5772/51253

1. Introduction

Recently, the wind generation systems are attracting attention as a clean and safe renewable energy source. Induction machines have many advantageous characteristics such as high robustness, reliability and low cost. Therefore, induction machines are used in high-performance applications, which require independent torque and flux control. The induction machines may be used as a motor or a generator. Self-excited induction generators (SEIG) are good candidates for wind-power electricity generation especially in remote areas, because they do not need an external power supplies to produce the excitation magnetic fields in [1–3]. The excitation can be provided by a capacitor bank connected to the stator windings of the induction generator. Magnetizing inductance is the main factor for voltage build-up of the IG. The minimum and maximum values of capacitance required for self-excitation have been analyzed previously in [4–7].

The three phase current regulated pulse-width modulation (CRPWM) AC/DC/AC converters have been increasingly used for wind energy system applications. Their attractive features include: regulated DC-link voltage, low harmonic distortion of the induction generator currents and controllable power factor and efficiency in [8–9]. The current regulation of a SEIG in the synchronous frame has the advantages of fast dynamic current response, good accuracy, constant switching frequency and less sensitivity to parameter variations. In wind generation systems, a variable speed generation system is more attractive than a fixed speed one because of the improvement in the wind energy production. In a variable speed system, wind turbine can be operated to produce its maximum power at every wind speed by adjusting the shaft speed optimally. In order to achieve the maximum power point tracking

(MPPT) control, some control schemes have been studied. For example, a search-based or perturbation-based strategy in [10–11], a fuzzy- logic based control in [12], a wind speed-estimation-based algorithm has been applied. Since the squirrel-cage IGs have robust construction, lower initial, run-time and maintenance cost, squirrel-cage IGs are suitable for grid-connected as well as isolated power sources in small hydroelectric and wind-energy applications. Therefore an IG system using radial basis function network (RBFN) was proposed to yield maximum power output through the DC-link power control in [13-14].

In the past several years, much research has been carried out in neural network control. It has proven that an artificial neural network can approximate a wide range of nonlinear functions to any desired degree of accuracy under certain conditions. In the conventional gradient descent method of weight adaptation, the sensitivity of the controlled system is required in the on-line training process. However, it is difficult to acquire sensitivity information for unknown or highly non-linear dynamics. Wavelets have been combined with the neural network to create wavelet–neural–networks (WNNs). It combine the capability of artificial neural networks for learning from process and the capability of wavelet decomposition for identification and control of dynamic systems. The training algorithms for WNN typically converge in a smaller number of iterations than the conventional neural networks. Unlike the sigmoid functions used in the conventional neural networks, the second layer of WNN is a wavelet form, in which the translation and dilation parameters are included. Thus, WNN has been proved to be better than the other neural networks in that the structure can provide more potential to enrich the mapping relationship between inputs and outputs in [15-23].

Particle swarm optimization (PSO), first introduced by Kennedy and Eberhart in [24], is one of the modern heuristic algorithm. It was developed through simulation of a simplified social system and has been found to be robust in solving continuous nonlinear optimization problem in [25-29]. The PSO technique can generate a high quality solution within shorter calculation time and stable convergence characteristics than other stochastic methods in [30-34]. Much research is still in progress for proving the potential of the PSO in solving complex dynamical systems.

The recent evolution of power-electronics technologies has aided the advancement of variable-speed wind-turbine generation systems in [35–39]. In spite of the additional cost of power electronics and control circuits, the total energy captured in a variable-speed wind-turbine system is more than the conventional one. Thus, the variable-speed wind-turbine system has lower life-cycle cost. Moreover, the PWM converters not only can be used as a variable capacitor but also can supply the needed reactive power to load and to minimize the harmonic current and imbalance in the generator current. On the other hand, the variable speed wind turbine driven SEIG systems display highly resonant, nonlinear, and time-varying dynamics subject to wind turbulence and operating temperature of the SEIG. Furthermore, there is an appreciable amount of fluctuation in the magnitude and frequency of the generator terminal voltage owing to a varying rotor speed governed by the wind velocity and the pulsating input torque from the wind turbine. The phenomena of fluctuation are objectionable to some sensitive loads. Therefore, the employment of PWM converters with advanced control methodologies to control the wind turbine driven SEIG systems is necessary in [36–38]. In addition, for the research of wind energy conversion systems, the developments of wind turbine emulators are also necessary in [43, 44]. However, the fuzzy logic controller, the sliding-mode controller, and the PI controller adopted in [40–48] may not guarantee the robustness when parameter variations or external disturbance occurred in the control system in practical applications due to the lack of online learning ability.

This Chapter is organized as follows. Section 2 presents the variable speed wind generation system description. In this section the analysis of the wind turbine is carried out and the maximum power point tracking analysis is also introduced. In Section 3, the dynamic model of the self-excited induction generator is introduced to analyze all its characteristics. Section 4 provides the indirect field-orientation control (IFOC) dynamics for the IG (torque, slip angular frequency and voltage commands) which are derived from the dynamic model of SEIG. The d-q axes current control according to the IG rotor speed gives the maximum mechanical power from the wind turbine and the losses of the IG are minimized. In Section 5, the dynamic equations of the CRPWM converter in the synchronous reference frame are carried out based on the IFOC dynamics of the IG. The dynamic equations of the grid-side CRPWM voltage source inverter connected to the grid are given in Section 6. By using vector control technique, the currents of the CRPWM inverter are controlled with very high bandwidth. The vector control approach is used, with a reference frame oriented along the grid voltage vector position. This allows independent control of the active and reactive power. Section 7 considers the design procedures for the PID voltage controller of the IG-side CRPWM voltage source converter, the PID active power and reactive power controllers for the grid-side CRPWM inverter. In Section 8, an intelligent maximization hybrid control system based on the WNN with IPSO is proposed in order to control the DC-link voltage of the IG-side CRPWM voltage source converter, active power and reactive power of the grid-side CRPWM voltage source inverter effectively based on the MPPT from the wind driven SEIG system. Finally, to testify the design of the proposed hybrid control system and MPPT control scheme, the variable speed wind generation system is simulated in Section 9. The dynamic performance of the system has been studied under different wind velocities. The simulation results are provided to demonstrate the effectiveness of the proposed hybrid control for variable speed wind generation system.

2. Variable Speed Wind Generation System Description

The proposed wind generation system is shown in Figure 1. The wind turbine is coupled to the shaft of a SEIG. The output of the SEIG is connected to a double-sided CRPWM voltage source converter connected to a utility grid.

2.1. Double-Sided Converter System

The voltage-fed double-sided converter scheme used in the proposed wind energy conversion system is shown in Figure 1. The variable frequency variable voltage power genertated is rectified by a PWM converter. The PWM inverter topology is identical to that of the PWM converter and it supplies the generated power to the utility grid. The converter consists of six switches with their anti-parallel diodes that are switched using space vector pulse width modulation (SVPWM) pattern. The switching functions of the top and bottom devices are defined S_a, S_b and S_c; and $S_a{}'$, $S_b{}'$ and $S_c{}'$ respectively. The switching function has a value of one when the switch is turned on and it is zero when it is turned off. The voltage equations for the converter in the stationary reference frame can be expressed in terms of the switching functions as given by (1-3).

$$V_a = \frac{1}{3} V_{dc}[2S_a - S_b - S_c] \tag{1}$$

$$V_b = \frac{1}{3} V_{dc}[-S_a + 2S_b - S_c] \tag{2}$$

$$V_c = \frac{1}{3} V_{dc}[-S_a - S_b + 2S_c] \tag{3}$$

2.2. Analysis of Wind Turbine

The wind turbine driven SEIG system has the following parameters. The Wind turbine parameters are P_m=1.5 kW at V_ω=16m/s, turbine radius R_T=0.7m and λ_{opt}=6.5 while the IG parameters are P_e=1.5 kW, V=380 V, I_s=4 A, number of poles P=4, f=50 Hz, R_s =6.29Ω, R_r = 3.59Ω, L_s =L_r =480 mH, L_m =464 mH and the total moment of inertia of the wind turbine and the IG J=2 kg. m^2.

The wind turbine is characterized by the non-dimensional curve of coefficient of performance as a function of tip-speed ratio λ. The mechanical input power P_m of a fixed-pitch wind turbine as a function of the effective wind velocity V_ω through the blades, the air density, ρ, the blades radius R_T and the power coefficient C_P is given in [9, 12]:

$$P_{mT} = \frac{1}{2} \rho \pi R_T^2 V_\omega^3 C_P(\lambda) \tag{4}$$

Considering the rotational speed of the wind turbine ω_t and the torque coefficient $C_T(\lambda)$, the wind turbine mechanical torque is given by:

$$T_{mT} = \frac{1}{2} \rho \pi R_T^3 V_\omega^2 C_T(\lambda) \tag{5}$$

$$C_P(\lambda) = \lambda C_T(\lambda) \tag{6}$$

where $C_P(\lambda)$ is the turbine power coefficient, $C_T(\lambda)$ is the turbine torque coefficient, V_ω is the wind velocity (in m/s), ρ is the air density (typically 1.25 kg/m^3), R_T is the blades radius (in m) and λ is tip-speed ratio and is defined as:

$$\lambda = \omega_T R_T / V_\omega \tag{7}$$

where ω_T is the wind turbine rotational speed (rad/s).

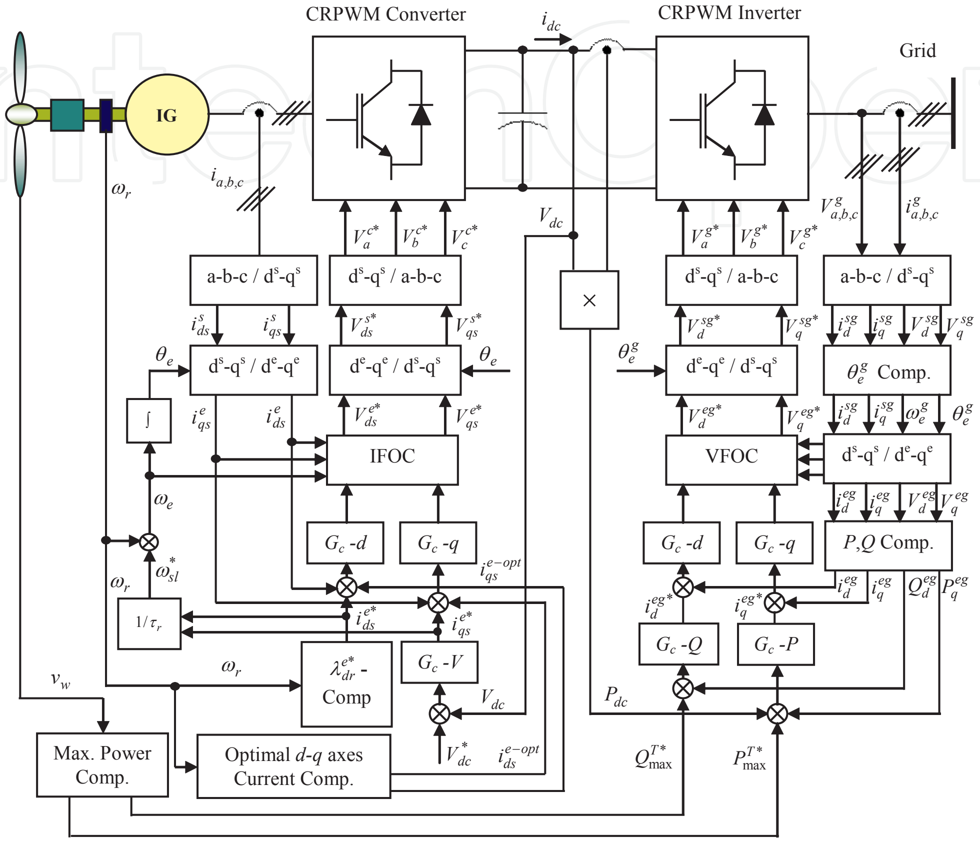

Figure 1. Intelligent maximization control of a variable speed wind driven self-excited induction generator system connected to a utility grid.

The turbine power coefficient $C_P(\lambda)$ and the turbine torque coefficient $C_T(\lambda)$ are functions of the tip-speed ratio of the blades if the pitch angle of the blade is constant. The turbine power coefficient is represented by various approximation expressions. In this Chapter, $C_P(\lambda)$ and $C_T(\lambda)$ are approximated by a fifth-order polynomial curve fit given by (8-9) and are shown in Figures (2 and 3). The power and torque versus speed curves of wind turbine can be calculated by (4)-(7) at various wind velocities. The optimum point corresponds to the condition where the power coefficient $C_P(\lambda)$ becomes the maximum. The maximum C_P is 0.37 when λ=6.7.

$$\begin{aligned} C_P(\lambda) &= 0.0084948 + 0.05186\lambda - 0.022818\lambda^2 \\ &+ 0.01191\lambda^3 - 0.0017641\lambda^4 + 7.484x10^{-5}\lambda^5 \end{aligned} \tag{8}$$

$$C_T(\lambda)=0.00066294+0.0091889\lambda-0.0026952\lambda^2 \\ +0.001688\lambda^3-0.00028374\lambda^4+1.3269x10^{-5}\lambda^5 \tag{9}$$

2.3. Maximum Power Point Tracking Analysis

When the tip speed ratio is controlled by the optimum value regardless of the wind speed, the maximum mechanical power is obtained from the wind turbine. The optimum speed of the IG for maximum power of the wind turbine is given by (10) and the maximum mechanical power and the optimal torque are given by (11) and (12).

$$\omega_{opt}=K_{\omega-opt}V_{\omega} \tag{10}$$

$$P_{Tm-\max}=K^{V}_{p-\max}V^{3}_{\omega} \tag{11}$$

$$T_{Tm-opt}=K^{V}_{T-opt}V^{2}_{\omega} \tag{12}$$

$$K^{V}_{p-\max}=\frac{1}{2}\rho\pi R^{2}_{T}C_{p,\max} \tag{13}$$

$$K^{V}_{T-opt}=\frac{1}{2}\rho\pi R^{3}_{T}C_{p,\max}\Big/\lambda_{opt} \tag{14}$$

$$K_{\omega-opt}=\lambda_{opt}/R_T \tag{15}$$

$$K^{\omega}_{p-\max}=K^{V}_{p-\max}\Big/(K_{\omega-opt})^3 \tag{16}$$

$$K^{\omega}_{T-opt}=K^{V}_{T-opt}\Big/(K_{\omega-opt})^2 \tag{17}$$

$$P_{Tm-\max}=K^{\omega}_{p-\max}\omega^{3}_{opt} \tag{18}$$

$$T_{Tm-opt}=K^{\omega}_{T-opt}\omega^{2}_{opt} \tag{19}$$

When the IG speed is always controlled at the optimum speed given in (10), the tip-speed ratio remains the optimum value and the maximum power point can be achieved. At any wind speed, we can calculate the optimum rotational speed of the IG from (10), and then the maximum mechanical power is calculated from (11). The maximum power is used as the reference power to the CRPWM converter in order to get the maximum load current.

From (10)-(17), the maximum power and optimal torque as function of the optimum rotational IG speed are calculated and given by (18)-(19). From Figure 4, it is clear that the maximum power can be achieved when the IG torque is controlled on the optimal torque curve according to the IG rotor speed.

$$T_{IG-opt} = -K_{T-opt}^{\omega-IG}\omega_r^2 \tag{20}$$

$$K_{T-opt}^{\omega-IG} = K_{T-opt}^{V} \Big/ G.(K_{\omega-opt})^2 \tag{21}$$

3. Dynamic Model of the Self-Excited Induction Generator

The dynamic model of the IG is helpful to analyze all its characteristics. The *d-q* model in the arbitrary reference frame provides the complete solution for dynamic analysis and control in [2-4]. The dynamic model is given by (22-24, 25).

$$\begin{bmatrix}0\\0\\0\\0\end{bmatrix} = \begin{bmatrix} (R_s + L_s\sigma\frac{d}{dt}) & \omega L_s\sigma & \frac{L_m}{L_r}\frac{d}{dt} & \frac{L_m}{L_r}\omega \\ -\omega L_s\sigma & (R_s + L_s\sigma\frac{d}{dt}) & -\omega\frac{L_m}{L_r} & \frac{L_m}{L_r}\frac{d}{dt} \\ -\frac{L_m}{L_r}R_r & 0 & \left(R_r\Big/L_r + \frac{d}{dt}\right) & (\omega-\omega_r) \\ 0 & -\frac{L_m}{L_r}R_r & -(\omega-\omega_r) & \left(R_r\Big/L_r + \frac{d}{dt}\right) \end{bmatrix} \begin{bmatrix} i_{qs}\\ i_{ds}\\ \lambda_{qr}\\ \lambda_{dr}\end{bmatrix} + \begin{bmatrix} V_{qs}\\ V_{ds}\\ V_{qr}\\ V_{dr}\end{bmatrix} \tag{22}$$

$$V_{qs} = \frac{1}{C}\int i_{qs}dt + V_{cq}\mid_{t=0} \tag{23}$$

$$V_{ds} = \frac{1}{C}\int i_{ds}dt + V_{cd}\mid_{t=0} \tag{24}$$

$$T_e = -\frac{3}{2}\frac{P}{2}\frac{L_m}{L_r}(\lambda_{dr}i_{qs} - \lambda_{qr}i_{ds}) \tag{25}$$

where, V_{qs}, V_{ds}, i_{qs}, and i_{ds} are the stator voltages and currents, respectively. v_{qr} and v_{dr} are the rotor voltages. λ_{qr} and λ_{dr} are the rotor fluxes. R_s, L_s, R_r and L_r are the resistance and the self inductance of the stator and the rotor, respectively. L_m is the mutual inductance.

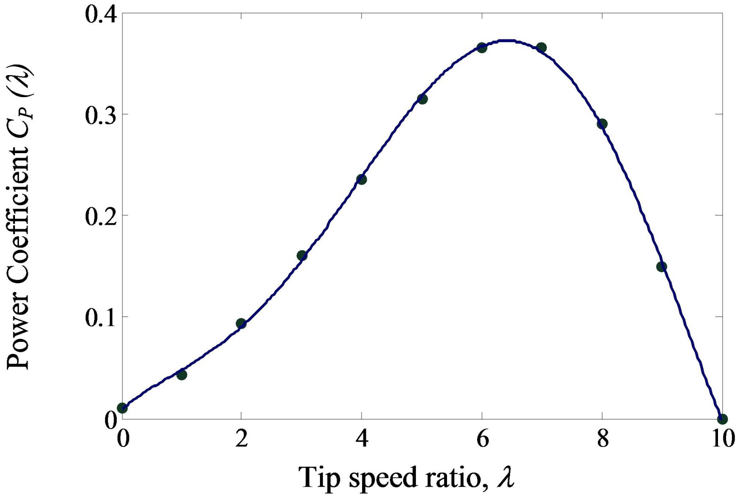

Figure 2. Power coefficient versus tip speed ratio.

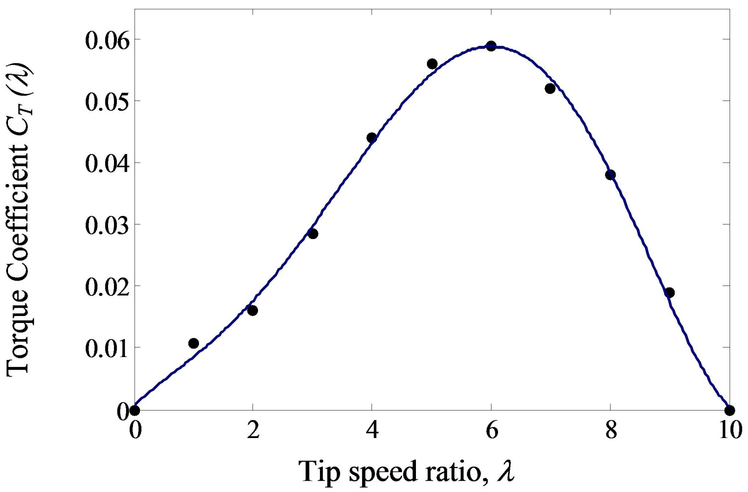

Figure 3. Torque coefficient versus tip speed ratio.

The relation between the wind turbine output torque and the electromagnetic torque of the IG is given by (26).

$$T_{Tm} = J\frac{d}{dt}\omega_m + \beta\omega_m + T_e \tag{26}$$

From (22-26), the state equations of the SEIG and wind turbine can be accomplished as in (27) and (28).

$$\frac{d}{dt}\omega_m = \frac{1}{J}T_{Tm} - \frac{\beta}{J}\omega_m - \frac{1}{J}T_e \tag{27}$$

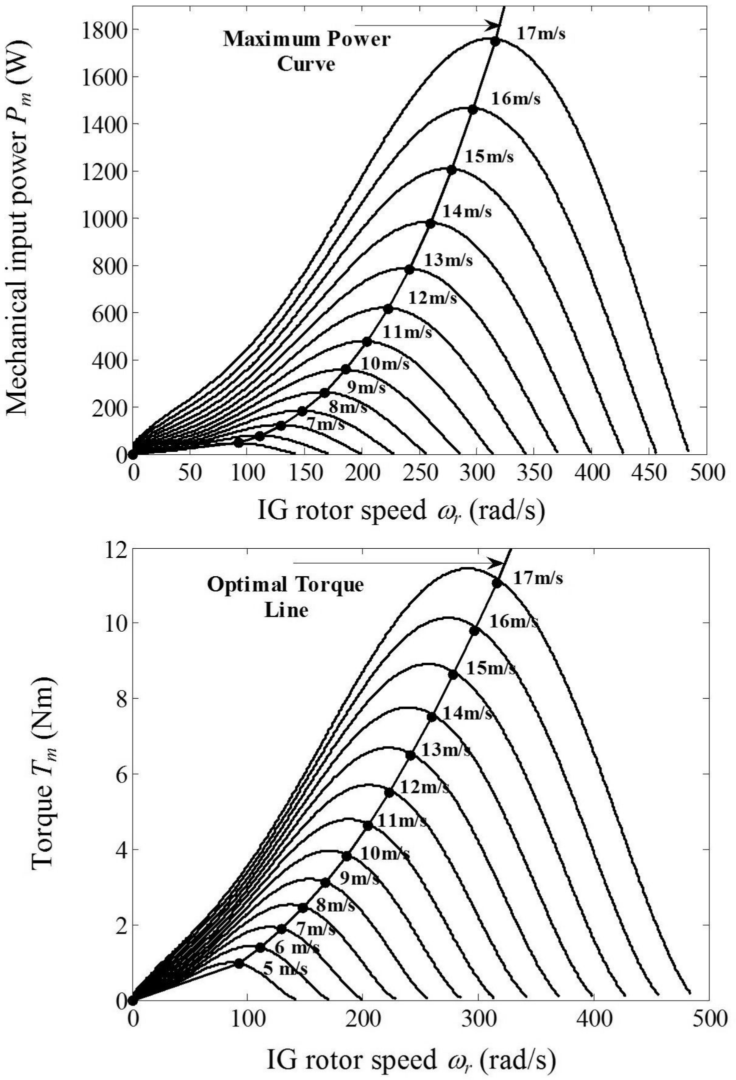

Figure 4. Characteristics of wind turbine at various wind speeds.

$$\frac{d}{dt}\begin{bmatrix} i_{qs} \\ i_{ds} \\ \lambda_{qr} \\ \lambda_{dr} \end{bmatrix} = \frac{1}{\sigma L_s L_r}\begin{bmatrix} -(R_s L_r + R_r L_m^2 / L_r) & -\omega\sigma L_s L_r & (L_m / L_r) R_r & -\omega_r L_m \\ \omega\sigma L_s L_r & -(R_s L_r + R_r L_m^2 / L_r) & \omega_r L_m & (L_m / L_r) R_r \\ \sigma L_s L_r L_m R_r / L_r & 0 & -\sigma L_s L_r R_r / L_r & -\sigma L_s L_r(\omega - \omega_r) \\ 0 & \sigma L_s L_r L_m R_r / L_r & \sigma L_s L_r(\omega - \omega_r) & -\sigma L_s L_r R_r / L_r \end{bmatrix}$$
$$\begin{bmatrix} i_{qs} \\ i_{ds} \\ \lambda_{qr} \\ \lambda_{dr} \end{bmatrix} + \frac{1}{\sigma L_s L_r}\begin{bmatrix} L_m v_{qr} - L_r v_{qs} \\ L_m v_{dr} - L_r v_{ds} \\ -\sigma L_s L_r v_{qr} \\ -\sigma L_s L_r v_{dr} \end{bmatrix} \tag{28}$$

where ω_m, J and β are the mechanical angular speeds of the wind turbine, the effective inertia of the wind turbine, the induction generator and the friction coefficient, respectively.

In order to model the induction machine when used for motoring application, it is important to determine the magnetizing inductance at rated voltage. In the SEIG, the variation of magnetizing inductance L_m is the main factor in the dynamics of voltage buildup and stabilization. In this investigation, the magnetizing inductance is calculated by driving the induction machine at synchronous speed and taking measurements when the applied voltage was varied from zero to 100% of the rated voltage. The magnetizing inductance used in this experimental setup is given as shown in Figure 5. The test results are based on the rated frequency (50 Hz) of the IG while the dots are experimental results and the curve is a fifth-order curve fit given by

$$L_m = -1.023\times 10^{-11} V_{ph}^5 + 6.162\times 10^{-9} V_{ph}^4 - 1.25\times 10^{-6} V_{ph}^3$$
$$+8.267\times 10^{-5} V_{ph}^2 - 3.843\times 10^{-5} V_{ph} + 0.1985$$

where V_{ph} is the phase voltage.

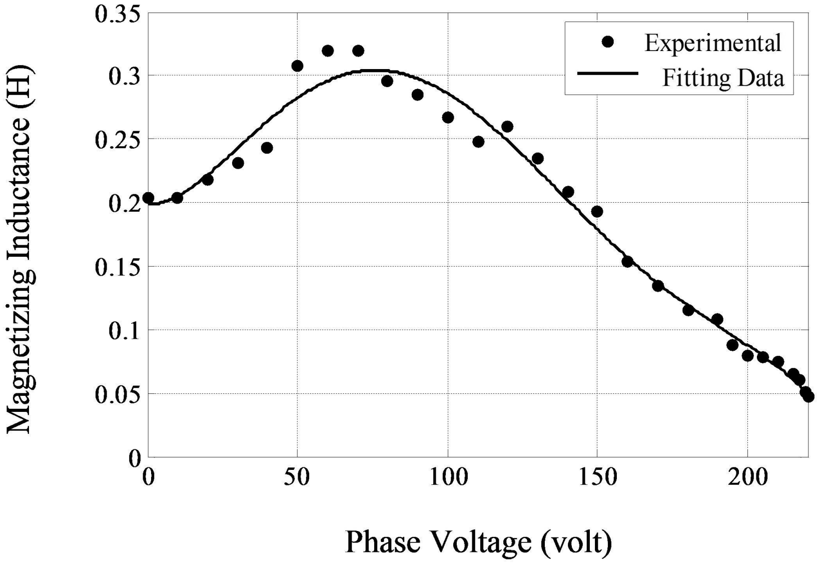

Figure 5. Magnetic curve of the SEIG.

4. Optimal IFOC of the Induction Generator

The IFOC dynamics for the IG can be derived from (22-25), respectively at λ_{qr}=0, $d\lambda_{qr}/dt$=0, $d\lambda_{dr}/dt$=0, and $\omega=\omega_e$. The torque and slip angular frequency for rotor field orientation are given in (26-27) while the voltage commands of the IFOC are given by (29-31) in [11, 12].

$$T_e = -K_t . i_{ds}^{e*} i_{qs}^{e*} = -K_{T-opt}^{\omega-IG} \omega_r^2 \tag{29}$$

$$\omega_{sl} = \frac{1}{\tau_r} \cdot \frac{i_{qs}^{e*}}{i_{ds}^{e*}} \tag{30}$$

$$\begin{bmatrix} V_{qs}^{e*} \\ V_{ds}^{e*} \end{bmatrix} = \begin{bmatrix} e_{qs}^{e} \\ e_{ds}^{e} \end{bmatrix} - \begin{bmatrix} R_s + \sigma L_s \frac{d}{dt} & \omega_e \sigma L_s \\ -\omega_e \sigma L_s & R_s + \sigma L_s \frac{d}{dt} \end{bmatrix} \begin{bmatrix} i_{qs}^{e} \\ i_{ds}^{e} \end{bmatrix} \tag{31}$$

where $K_t=(3/2)(P/2)(L_m)^2/L_r$ is the torque constant, e^e_{qs} and e^e_{ds} are the back EMFs of the IG. T_e, τ_r, ω_{sl}, and ω_e are the electromagnetic torque, the rotor time constant, the slip angular frequency, and the angular frequency of the synchronous reference frame, respectively.

$$\begin{bmatrix} e_{qs}^{e} \\ e_{ds}^{e} \end{bmatrix} = \begin{bmatrix} \omega_e \lambda_{dr}^{e} \frac{L_m}{L_r} \\ 0 \end{bmatrix} \tag{32}$$

In the previous analysis, the IG torque is given by (29) as a function of the rotor speed. Therefore, the d-axes current becomes a function only of the rotor speed. The optimal d-q axes currents i_{ds} and i_{qs} can be derived from (22) and (29) and are plotted as given in Figure 6. These plots show the relation of the optimal currents as function of the IG rotor speed and can be approximated by a third-order polynomials given by (34, 35).

$$i_{ds}^{e}(\omega_r) i_{qs}^{e}(\omega_r) = (K_{T-opt}^{\omega} / K_t)\omega_r^2 \tag{33}$$

$$i_{ds}^{e-opt}(\omega_r) = K_{d3}\omega_r^3 + K_{d2}\omega_r^2 + K_{d1}\omega_r + K_{d0} \tag{34}$$

$$i_{qs}^{e-opt}(\omega_r) = K_{q3}\omega_r^3 + K_{q2}\omega_r^2 + K_{q1}\omega_r + K_{q0} \tag{35}$$

By controlling the d-q axes currents utilizing (34)-(35) according to the IG rotor speed, the maximum mechanical power is obtained from the wind turbine and the losses of the IG are minimized. Also, from (29), it is clear that the IG torque is proportional to the q-axis current when the d-axis current is kept constant and thus he IG power is almost proportional to q-axis current. Therefore, the control of generated power becomes possible by adjusting the q-axis current according to the required generated power, where the d-axis current is given by (34).

5. Dynamic Model of the IG-Side CRPWM Voltage Source Converter

The block diagram of the CRPWM voltage source converter control system based on the IFOC-SEIG is shown in Figure 8. It is well known that the IFOC of induction machines allows for the independent control of two input variables, stator q-axis current i^e_{qs} and stator d-axis current i^{e}_{ds}. This suggests that it is possible to control the output voltage and power factor and/or efficiency by controlling the two components of the stator currents. The dynamic equations of the CRPWM converter are based on the IFOC dynamics of the IG in [12-14] and are given by (36, 37).

$$e^{e}_{qs} - V^{ec}_{qs} = R_s i^{ec}_{qs} + \sigma L_s \frac{d}{dt} i^{ec}_{qs} + \omega_e \sigma L_s i^{ec}_{ds} \tag{36}$$

$$e^{e}_{ds} - V^{ec}_{ds} = R_s i^{ec}_{ds} + \sigma L_s \frac{d}{dt} i^{ec}_{ds} - \omega_e \sigma L_s i^{ec}_{qs} \tag{37}$$

By considering the converter as an ideal current regulated source, the energy is transferred between the IG and the DC-link. As a consequence, the instantaneous power of both the converter's AC-side and DC-side is the same.

$$V_{dc} i_{dc} = \frac{3}{2}\left(V^{e}_{qs} i^{e}_{qs} + V^{e}_{ds} i^{e}_{ds}\right) \tag{38}$$

From (38), the relation between the DC-link current i_{dc} and the d-q axis currents i^{e}_{qs} and i^{e}_{ds} is as follows.

$$i_{dc} = \frac{3}{2}\left(\frac{V^{e}_{qs}}{V_{dc}} i^{e}_{qs} + \frac{V^{e}_{ds}}{V_{dc}} i^{e}_{ds}\right) \tag{39}$$

At FOC $V^{e}_{ds} \cong 0$, therefore, there is a direct relation between the DC-link current and the q-axis current of the IG.

$$i^{e}_{qs} = \frac{2}{3} \frac{V_{dc}}{V^{e}_{qs}} i_{dc} \tag{40}$$

The dynamics of the DC-link is given by (41-43).

$$C_{dc} \frac{d}{dt} V_{dc} + i_L = i_{dc} \tag{41}$$

$$C_{dc} \frac{d}{dt} V_{dc} + \frac{1}{R_L} V_{dc} = i_{dc} \tag{42}$$

$$i_{dc} = \frac{3}{2} \frac{V^{e}_{qs}}{V_{dc}} i^{e}_{qs} \tag{43}$$

where, C_{dc} is the DC-link capacitor, i_L is the load current and i_{dc} is the DC-link current. The state equations of the CRPWM converter and DC-link are derived from (36-43) and are given in (44-45).

$$\frac{d}{dt}V_{dc} = \begin{bmatrix} \frac{1}{C_{dc}} & -\frac{1}{R_L\ C_{dc}} \end{bmatrix} \begin{bmatrix} i_{dc} \\ V_{dc} \end{bmatrix} \tag{44}$$

$$\begin{aligned} \frac{d}{dt}\begin{bmatrix} i_{qs}^{ec} \\ i_{ds}^{ec} \\ V_{dc} \end{bmatrix} &= \frac{1}{\sigma L_s}\begin{bmatrix} -R_s & \omega_e \sigma L_s & 0 \\ -\omega_e \sigma L_s & R_s & 0 \\ \sigma L_s K_{dc}^q & \sigma L_s K_{dc}^d & 0 \end{bmatrix}\begin{bmatrix} i_{qs}^{ec} \\ i_{ds}^{ec} \\ V_{dc} \end{bmatrix} \\ &+ \frac{1}{\sigma L_s}\begin{bmatrix} \sigma L_s & 0 & 0 \\ 0 & \sigma L_s & 0 \\ 0 & 0 & -\sigma L_s \end{bmatrix}\begin{bmatrix} e_{qs}^{e} - V_{qs}^{ec} \\ e_{ds}^{e} - V_{ds}^{ec} \\ i_L \end{bmatrix} \end{aligned} \tag{45}$$

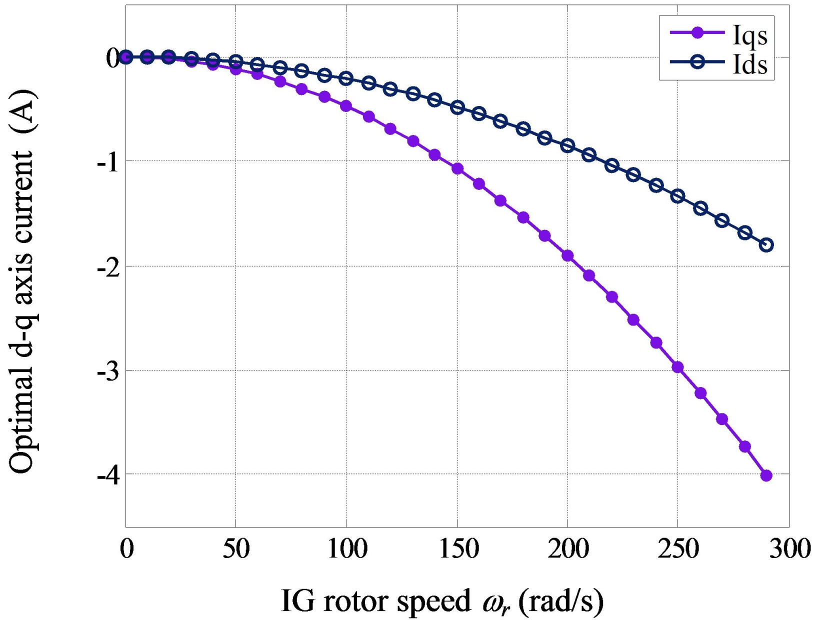

Figure 6. Optimal d-q axes currents as a function of IG rotor speed.

From (45), the current in q-axis i_{qs}^e can be estimated as:

$$i_{qs}^{e} = A_n^{-1}[\dot{V}_{dc} - B_n i_L\ - C_n E_{qds}^{e}] \tag{46}$$

where, $A_n = [K_{dc}^q + K_{dc}^d / \tau_r . \omega_{sl}]$, $B_n = [-1/C_{dc}]$, $C_n = [1/C_{dc}]$ and $E_{qds}^e = [e_{qs}^{e*} - V_{qs}^{e*}\quad e_{ds}^{e*} - V_{ds}^{e*}]$.

At the steady state, the load current i_L is approximately equals to the DC-link current i_{dc}. Therefore, the optimal load current can be approximated by (47). Figure 7 shows the optimal load current corresponding to the maximum mechanical power obtained from the wind turbine.

$$i_L^{opt}(\omega_r) = K_{L\ 3}\omega_r^3 + K_{L\ 2}\omega_r^2 + K_{L\ 1}\omega_r + K_{L\ 0} \tag{47}$$

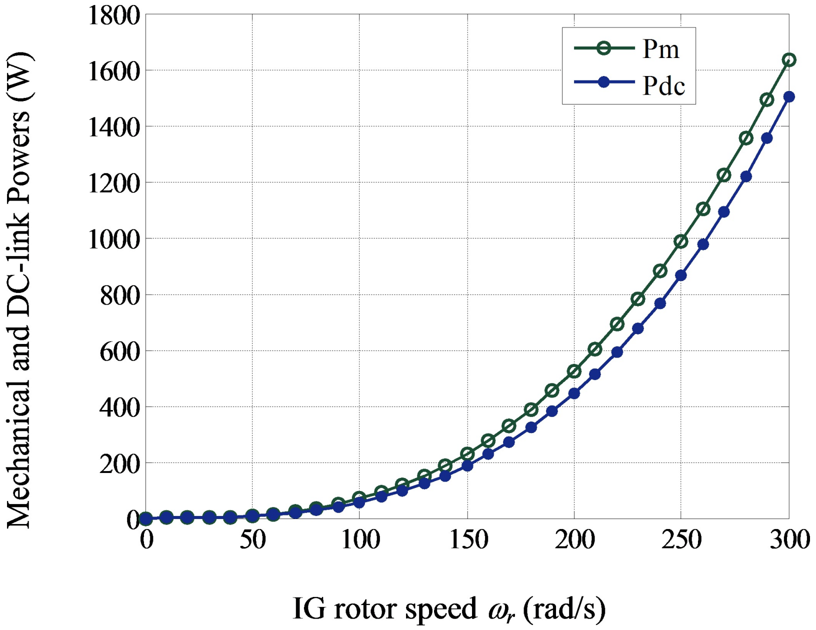

Figure 7. Optimal load current as a function of IG rotor speed.

6. Dynamic Model of the Grid-Side CRPWM Voltage Source Inverter

The grid-side CRPWM voltage source inverter is connected to the grid through three single-phase coils (control windings). With this configuration it is possible to operate using boost mode and have attractive features as constant DC–link voltage, low harmonic distortion of grid current, bidirectional power flow and adjustable power factor. The aim of the control of the grid-side CRPWM voltage source converter is to impose a current to the control winding and to control independently the active and reactive power to be injected to the grid. By using vector control technique, the currents of the CRPWM inverter are controlled with very high bandwidth. The vector control approach is used, with a reference frame oriented along the grid voltage vector position, such that $V_{qg} = V_{mg}$ and $V_{dg} = 0$. This allows independent control of the active and reactive power through currents i_{qg} and i_{dg} respectively. Usually, the reactive power component current is set to zero for unity power factor operation. The primary aim of this control scheme is to modulate the inverter to regulate the magnitude and the phase angle of the grid supply current, so that the active and reactive power entering the network can be controlled. The procedure for modeling the CRPWM inverter is based on the virtual-flux orientation control (VFOC) technique. The grid-side converter control, shown in Figure 9, is based on the d–q voltage equations of the grid-reactance-converter system according to following equations:

$$\begin{bmatrix} V_q^{eg*} \\ V_d^{eg*} \end{bmatrix} = \begin{bmatrix} e_q^{eg} \\ e_d^{eg} \end{bmatrix} + \begin{bmatrix} R_g + L_g p & \omega_{\mathrm{eg}} L_g \\ -\omega_{\mathrm{eg}} L_g & R_g + L_g p \end{bmatrix} \begin{bmatrix} i_q^{eg} \\ i_d^{eg} \end{bmatrix} \tag{48}$$

$$\begin{bmatrix} P \\ Q \end{bmatrix} = \frac{3}{2} \cdot \begin{bmatrix} V_q^{eg} & V_d^{eg} \\ V_d^{eg} & -V_q^{eg} \end{bmatrix} \begin{bmatrix} i_q^{eg} \\ i_d^{eg} \end{bmatrix} \tag{49}$$

The vector control of the grid-side CRPWM inverter is represented in the block diagram illustrated in Figure 9. The control of the reactive power is realized by acting over the control winding current, i_{ds}. The reference current is obtained by a PI current controller that adjusts the reactive power to a desired amount. Similarly, the control of the active power is realized by acting over the control winding current i_{qs} and the reference current is given by a PI current controller. The possible situation for defining the current references is to track the maximum turbine power for each wind speed.

At VFOC, $V_{dg} = 0$. Therefore, there are a direct relations between the active power, P and q–axis current and the reactive power, Q and d–axis current of the control windings. This allows independent control of the active and reactive power through currents i_{qg} and i_{dg} respectively according to following equations:

$$\begin{bmatrix} P \\ Q \end{bmatrix} = \frac{3}{2} \cdot \begin{bmatrix} +V_q^{eg} & 0 \\ 0 & -V_q^{eg} \end{bmatrix} \begin{bmatrix} i_q^{eg} \\ i_d^{eg} \end{bmatrix} \tag{50}$$

The d-q current commands of the inverter are expressed as:

$$\begin{bmatrix} i_q^{eg*} \\ i_d^{eg*} \end{bmatrix} = \frac{2}{3} \begin{bmatrix} +\dfrac{P^*}{V_q^{eg*}} \\ -\dfrac{Q^*}{V_q^{eg*}} \end{bmatrix} \tag{51}$$

where, P^* and Q^* denote the required maximum active and reactive power. To achieve the unity power factor operation, Q^* must be zero. From (50), it is obvious that the current command of the d–axis must be zero for unity power factor operation and the current command of the q–axis can be evaluated from the required active power. It is seen from (47) that coupling terms exist in the d-q current control loops. The d–q voltage decouplers are designed to decouple the current control loops. Suitable feed-forward control components of grid voltages are also added to speed up current responses. The d-q current control loops of the CRPWM inverter in the proposed control system are shown in Figure 9.

7. Design of the PID Controllers for Double-Sided CRPWM AC/DC/AC Voltage Source Converters

This section considers the design procedures for the PID voltage controller of the IG-Side CRPWM voltage source converter, the PID active power and reactive power controllers for the grid-side CRPWM inverter. The design procedures are based on the integral time absolute error (ITAE) performance index response method to obtain the desired control performance in the nominal condition of command tracking.

7.1. PID Voltage Controller Design for IG-Side CRPWM Voltage Source Converter

A systematic design procedure for the PI current controllers capable of satisfying the desired specifications is given in [12]. The gains of the PI d-q axis current controllers have been determined using the ITAE performance index response method and are given by (51-52). From the block diagram shown in Figure 8, a back EMF estimator is adopted to q-axis current loop for voltage feed-forward control. The q-axis stator current of the IG is selected as the variable to be changed to regulate the DC-link voltage. The voltage control is carried out through a voltage control loop using a PID voltage controller and is designed to stabilize the voltage control loop. The gains of the PID controller have been determined using the ITAE performance index response method. By exercising the decoupling control, the dynamic model including the CRPWM converter and the IG can be simplified and the closed loop transfer function is given by (53) from Figure 7.

$$\begin{aligned} K_i^{cq} &= \omega_n^2 \sigma L_s \\ K_p^{cq} &= (1.4\omega_n \sigma L_s - R_s - T_q) \end{aligned} \tag{52}$$

$$\begin{aligned} K_i^{cd} &= \omega_n^2 \sigma L_s \\ K_p^{cd} &= (1.4\omega_n \sigma L_s - R_s - T_d) \end{aligned} \tag{53}$$

$$\begin{aligned} \left.\frac{V_{dc}(s)}{V_{dc}^*(s)}\right|_{i_L=0} &= \frac{a_3 s^3 + a_2 s^2 + a_1 s + a_0}{s^4 + b_3 s^3 + b_2 s^2 + b_1 s + b_0} \\ &\cong \frac{\omega_n^4}{s^4 + 2.1\omega_n s^3 + 3.4\omega_n^2 s^2 + 2.7\omega_n^3 s + \omega_n^4} \end{aligned} \tag{54}$$

The PID voltage controller parameters are given by (54-56).

$$K_P^{v}=\frac{1}{K_{dc}}.\frac{\sigma L_{s}}{K_i^{cq}}\left(2.7\omega_n^3-\frac{K_p^{cq}}{K_i^{cq}}.\omega_n^4\right) \tag{55}$$

$$K_i^{v}=\frac{1}{K_{dc}}.\frac{\sigma L_{s}}{K_i^{cq}}.\omega_n^4 \tag{56}$$

$$K_d^{v}=\frac{1}{K_{dc}}.\frac{\sigma L_{s}}{K_i^{cq}}.\left(\omega_n^4.\frac{K_p^{cq}}{K_i^{cq}}-2.7\omega_n^3.\frac{K_p^{cq}}{K_i^{cq}}+3.4\omega_n^2-\frac{K_i^{cq}}{\sigma L_{s}}\right) \tag{57}$$

7.2. PID Active Power Controller Design for Grid-Side CRPWM Voltage Source Inverter

A systematic design procedure for the PI current controllers is given in [12]. These controllers are designed based on the control windings dynamic model at VFOC. The gains of the PI d-q axis current controllers have been determined and are given by (57-58). The q-axis current of the control winding is selected as the variable to be changed to regulate the active power, *P*. The active power control is carried out through a power control loop using a PID controller and is designed to stabilize the active power control loop. The gains of the PID controller have been determined using the ITAE method. The block diagram of the active power control loop is shown in Figure 9. The closed loop transfer function of the active power control loop is given by (59).

$$\begin{aligned}K_i^{gq}&=\omega_n^2L_{g}\\K_p^{gq}&=(1.4\omega_nL_{g}-R_g)\end{aligned} \tag{58}$$

$$\begin{aligned}K_i^{gd}&=\omega_n^2L_{g}\\K_p^{gd}&=(1.4\omega_nL_{g}-R_g)\end{aligned} \tag{59}$$

$$\left.\frac{P_q^{eg}(s)}{P_{\max}^{T*}(s)}\right|_{VFOC}=\frac{c_3^Ps^3+c_2^Ps^2+c_1^Ps+c_0^P}{s^3+d_2^Ps^2+d_1^Ps+d_0^P}\cong\frac{\omega_n^3}{s^3+1.75\omega_ns^2+2.15\omega_n^2s+\omega_n^3} \tag{60}$$

The PID controller parameters are given by (60-62).

$$K_d^P=\frac{\left(1.75\omega_nL_{g}K_i^{qg}-R_gK_i^{qg}-2.15\omega_n^2L_{g}K_p^{qg}\right)}{\left(K_q^PK_i^{2qg}+2.15\omega_n^2K_q^PK_p^{2qg}-1.75\omega_nK_q^PK_p^{qg}\right)} \tag{61}$$

$$K_p^P=\left(\frac{2.15\omega_n^2L_{g}}{K_q^PK_i^{qg}}\right)-\frac{1}{K_q^P}+\left(2.15\omega_n^2\frac{K_p^{qg}}{K_i^{qg}}\right).K_d^P \tag{62}$$

$$K_i^P = \left(\frac{\omega_n^3 L_g}{K_q^P K_i^{qg}} \right) + \left(\frac{K_p^{qg}}{K_i^{qg}} \right) . K_d^P \tag{63}$$

7.3. PID Reactive Power Controller Design for Grid-Side CRPWM Voltage Source Inverter

Similarly, the PID reactive power controller is designed and analyzed. The d-axis current of the control winding is selected as the variable to be used to regulate the reactive power, Q. The block diagram of the reactive power control loop is shown in Figure 9. The closed loop transfer function of the reactive power control loop is given by:

$$\left. \frac{Q_d^{eg}(s)}{Q_{\max}^{T*}(s)} \right|_{VOC} = \frac{c_3^Q s^3 + c_2^Q s^2 + c_1^Q s + c_0^Q}{s^3 + d_2^Q s^2 + d_1^Q s + d_0^Q} \cong \frac{\omega_n^3}{s^3 + 1.75\omega_n s^2 + 2.15\omega_n^2 s + \omega_n^3} \tag{64}$$

The PID controller parameters are given by (64-66).

$$K_d^Q = \frac{\left(1.75\omega_n L_g K_i^{dg} - R_g K_i^{dg} - 2.15\omega_n^2 L_g K_p^{qg}\right)}{\left(K_q^Q K_i^{2dg} + 2.15\omega_n^2 K_q^Q K_p^{2dg} - 1.75\omega_n K_q^Q K_p^{dg}\right)} \tag{65}$$

$$K_p^Q = \left(\frac{2.15\omega_n^2 L_g}{K_q^Q K_i^{dg}} \right) - \frac{1}{K_q^Q} + \left(2.15\omega_n^2 \frac{K_p^{dg}}{K_i^{dg}} \right) . K_d^Q \tag{66}$$

$$K_i^Q = \left(\frac{\omega_n^3 L_g}{K_q^Q K_i^{dg}} \right) + \left(\frac{K_p^{dg}}{K_i^{dg}} \right) . K_d^Q \tag{67}$$

8. Intelligent Maximization Control for Double-Sided CRPWM AC/DC/AC Voltage Source Converters

8.1. Configuration of the Proposed Intelligent Maximization Control System

In order to control the DC-link voltage of the IG-side CRPWM voltage source converter, active power and reactive power of the grid-side CRPWM voltage source inverter effectively, an intelligent maximization hybrid control system is proposed. The configuration of the proposed hybrid control system, which combines an on-line trained wavelet-neural-network controller (WNNC) with IPSO and a PID compensator, for wind turbine generation system is illustrated in Figures (8 and 9). It basically consists of an PI current controllers in the d-q axis, a three PID controllers and three on-line trained WNNCs with IPSO in parallel with the three PID controllers for voltage control of the DC-link side of the CRPWM converter, active power and reactive power of the grid connected CRPWM inverter. Although the desired tracking and regulation characteristics for DC-link voltage, active power and reactive power can be obtained using the PID controllers with nominal parameters, the performance of the system is still sensitive to parameter variations. To solve this problem, a hybrid controller combining the PID controller and the WNNC with IPSO is proposed for the DC-link voltage, active power and reactive power for the double-sided CRPWM AC/DC/AC converters. The control law and error signals are designed as:

$$U_{qs}^{*} = U_{qs}^{*WNNC} + U_{qs}^{*PID} \tag{68}$$

$$i_{qs}^{e*} = \delta i_{qs}^{e*WNNC} + i_{qs}^{e*PID} \tag{69}$$

$$i_{ds}^{e*} = \delta i_{ds}^{e*WNNC} + i_{ds}^{e*PID} \tag{70}$$

$$\begin{aligned} e_v &= (V_{dc}^{*} - V_{dc}) \\ \dot{V}_{dc} &= k_v dV_{dc} / dt \end{aligned} \tag{71}$$

$$\begin{aligned} e_P &= (P^{*} - P) \\ \dot{P} &= k_P dP / dt \end{aligned} \tag{72}$$

$$\begin{aligned} e_Q &= (Q^{*} - Q) \\ \dot{Q} &= k_Q dQ / dt \end{aligned} \tag{73}$$

where i_{qs}^{e*PID} is the q-axis current command generated from the PID controller and δi_{qs}^{e*WNNC} is produced by the proposed WNNC with IPSO to automatically compensate for performance degradation.

$i_{qs}^{e*PID} = i_{qs}^{eg*PID}$ for CRPWM inverter, $i_{qs}^{e*PID} = i_{qs}^{e*PID}$ for CRPWM converter, $i_{ds}^{e*PID} = i_{ds}^{eg*PID}$ for CRPWM inverter, $\delta i_{qs}^{e*WNNC} = \delta i_{qs}^{eg*WNNC}$ for CRPWM inverter, $\delta i_{qs}^{e*WNNC} = \delta i_{qs}^{e*WNNC}$ for CRPWM converter, $i_{ds}^{e*WNNC} = i_{ds}^{eg*WNNC}$ for CRPWM inverter, $P^{*} = P_{\max}^{T*}$ for CRPWM inverter, $Q^{*} = Q_{\max}^{T*}$ for CRPWM inverter.

8.2. Wavelet–Neural–Network Controller with IPSO

Since the squirrel-cage IGs have robust construction and lower initial, run time and maintenance cost squirrel-cage IGs are suitable for grid-connected in wind-energy applications. Therefore, a WNNC with IPSO is proposed to control a SEIG system for grid-connected wind-energy power application. The on-line trained WNNC with IPSO combines the capability of artificial neural-network for learning ability and the capability of wavelet decomposition for identification ability. Three on-line trained WNNCs with IPSO are introduced as the regulating controllers for both the DC-link voltage of the CRPWM AC/DC converter, active and reactive power of the CRPWM DC/AC grid-connected inverter. In addition, the on-line training algorithm based on the backpropagation is derived to train the connective weights, translations and dilations in the WNNs on-line. Furthermore, an IPSO is adopted to optimize the learning rates to further improve the on-line learning capability of the WNN and hence the improvement of the control performance can be obtained.

8.3. Wavelet–Neural–Network Structure

The architecture of the proposed four-layers WNN in [15-23] is shown in Figure 10, which comprises an input layer (the *i* layer), a mother wavelet layer (the *j* layer), a wavelet layer (the *k* layer) and an output layer (the *o* layer), is adopted to implement the WNNC. The signal propagation and the basic function in each layer are introduced as follows.

1. *Layer 1: Input Layer*

The nodes in layer 1 transmit the input signals to the next layer. The input variables are the error signal, $e(t)$, and the rate of change of the DC-link voltage, active power and reactive power. For every node *i* in the input layer, the input and the output of the WNN can be represented as:

$$net_i^1 = x_i^1, \quad y_i^1 = f_i^1(net_i^1) = net_i^1 \;\; i = 1,\, 2 \tag{74}$$

$$x_1^1 = e(t) and\, x_2^1 = \psi(t) \tag{75}$$

where $e(t) = e_v(t) = (V_{dc}^* - V_{dc})$ for the CRPWM converter, $e(t) = e_P(t) = (P^* - P)$, $e(t) = e_Q(t) = (Q^* - Q)$, $\psi(t) = \dot{V}_{dc}$, $\psi(t) = \dot{P}$, for the CRPWM inverter.

2. *Layer 2: Mother Wavelet Layer*

A family of wavelets is constructed by translations and dilations performed on the mother wavelet. In the mother wavelet layer each node performs a wavelet ϕ_j that is derived from its mother wavelet. There are many kind of wavelets that can be used in WNN. In this Chapter, the first derivative of the Gaussian wavelet function $\varphi(x) = -x\exp(-x^2/2)$, is adopted as a mother wavelet. For the *j*th node

$$net_j^2 = -(x_i^2 - \mu_{ij}) / \sigma_{ij}, \; y_j^2 = f_j^2(net_j^2) = \varphi_j(net_j^2)\, j = 1, \ldots, n \tag{76}$$

where μ_{ij} and σ_{ij} are the translation and dilations in the *j*th term of the *i*th input x_i^2 to the node of mother wavelet layer and *n* is the total number of the wavelets with respect to the input nodes.

3. *Layer 3: Wavelet Layer*

Each node *k* in layer 3 (wavelet layer) is denoted by $\prod$, which multiplies the incoming signal and outputs the result of the product. For the *k*th nodes:

$$net_k^3 = \prod_j \varpi_{jk}^3 x_j^3, \ y_k^3 = f_k^3(net_k^3) = net_k^3 \quad k = 1, \ldots\ldots, m \tag{77}$$

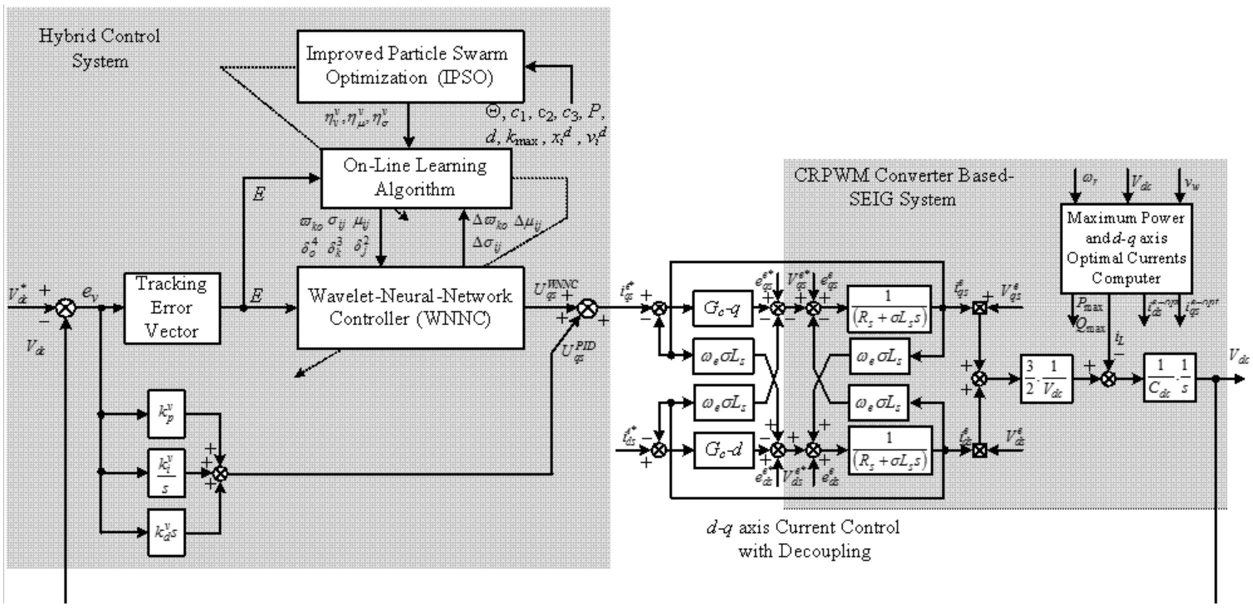

Figure 8. Integrated block diagram of the generator-side IFOC CRPWM voltage source converter using WNNC with IPSO control system.

where x_j^3 represents the *j*th input to the node of the wavelet layer (layer 3), ϖ_{jk}^3 is the weights between the mother wavelet layer and the wavelet layer. These weights are also assumed to be unity; and $m = (n / i)$ is the number of wavelets if each input node has the same mother wavelet nodes.

4. *Layer 4: Output Layer*

The single node *o* in the output layer is denoted by $\sum$, which computes the overall output as the summation of all incoming signals to obtain the final results.

$$net_o^4 = \sum_k^m \varpi_{ko}^4 x_k^4, \ y_o^4 = f_o^4(net_o^4) = net_o^4 \ o = 1 \tag{78}$$

$$y_o^4 = U_{qs}^{*WNNC}(t) = \delta i_{qs}^{e*WNNC}(t) \tag{79}$$

where the connecting weight ϖ_{ko}^4 is the output action strength of the *o*th output associated with the *k*th wavelet and x_k^4 represents the *k*th input to the node of output layer. The control problem is to design the WNNC to improve the convergence of the tracking error for the wind system.

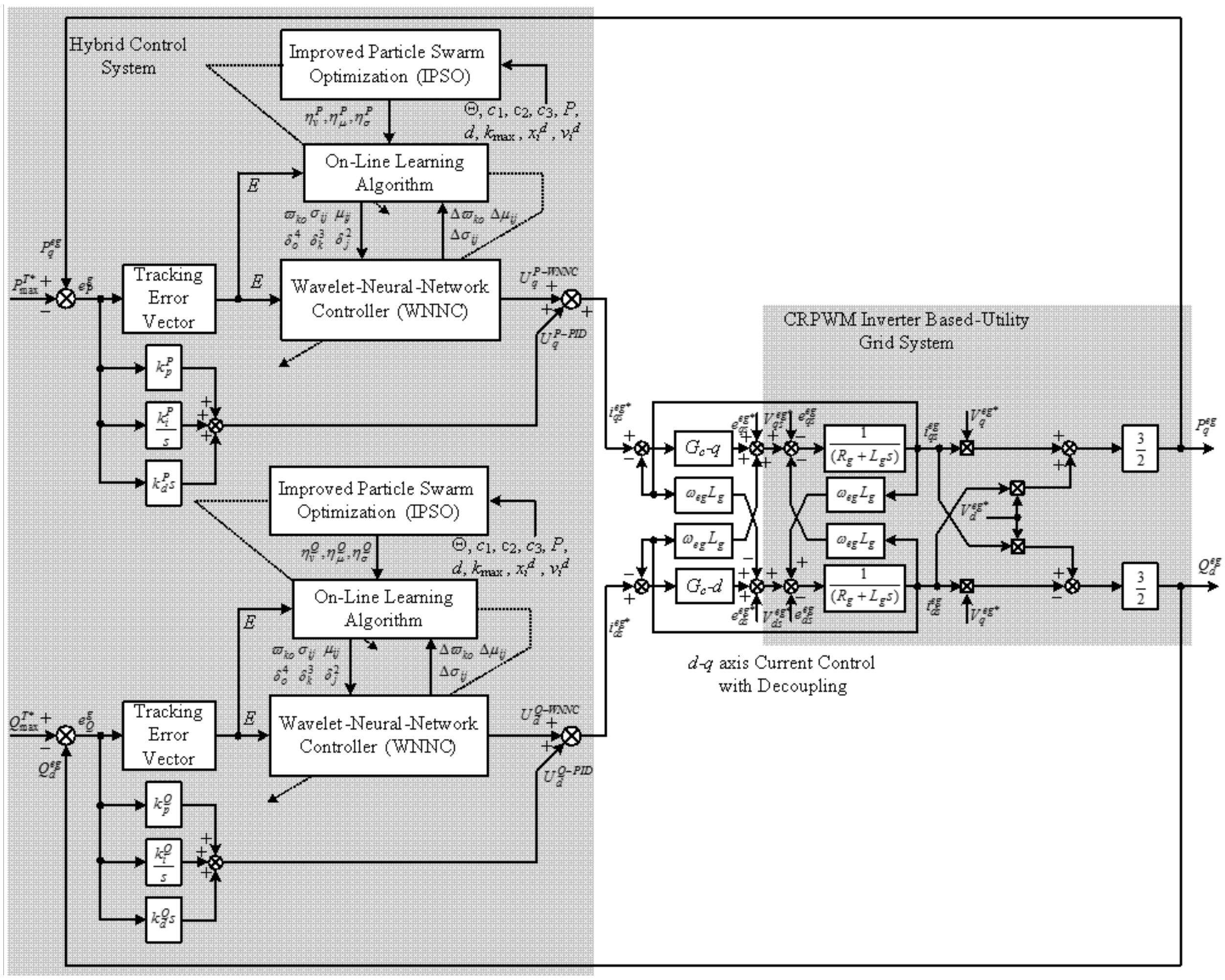

Figure 9. Integrated block diagram of the grid-side VFOC CRPWM voltage source inverter intelligent control system.

8.4. On-Line Training Algorithm Signal Analysis for WNNC

The essential part of the learning algorithm for an WNN concerns how to obtain a gradient vector in which each element in the learning algorithm is defined as the derivative of the energy function with respect to a parameter of the network using the chain rule. Since the gradient vector is calculated in the direction opposite to the flow of the output of each node, the method is generally referred to back-propagation learning rule in [15-23]. To describe the on-line learning algorithm of the WNNC using the supervised gradient descent method, the energy function is chosen as:

$$E = (1/2)(e)^2 \tag{80}$$

In the output layer (layer 4), the error term to be propagated is calculated as:

$$\delta_o^4 = -\frac{\partial E}{\partial net_o^4} = -\frac{\partial E}{\partial y_o^4}\cdot\frac{\partial y_o^4}{\partial net_o^4} = -\frac{\partial E}{\partial e}\cdot\frac{\partial e}{\partial net_o^4} = -\frac{\partial E}{\partial e}\cdot\frac{\partial e}{\partial \psi}\cdot\frac{\partial \psi}{\partial net_o^4} \qquad (81)$$

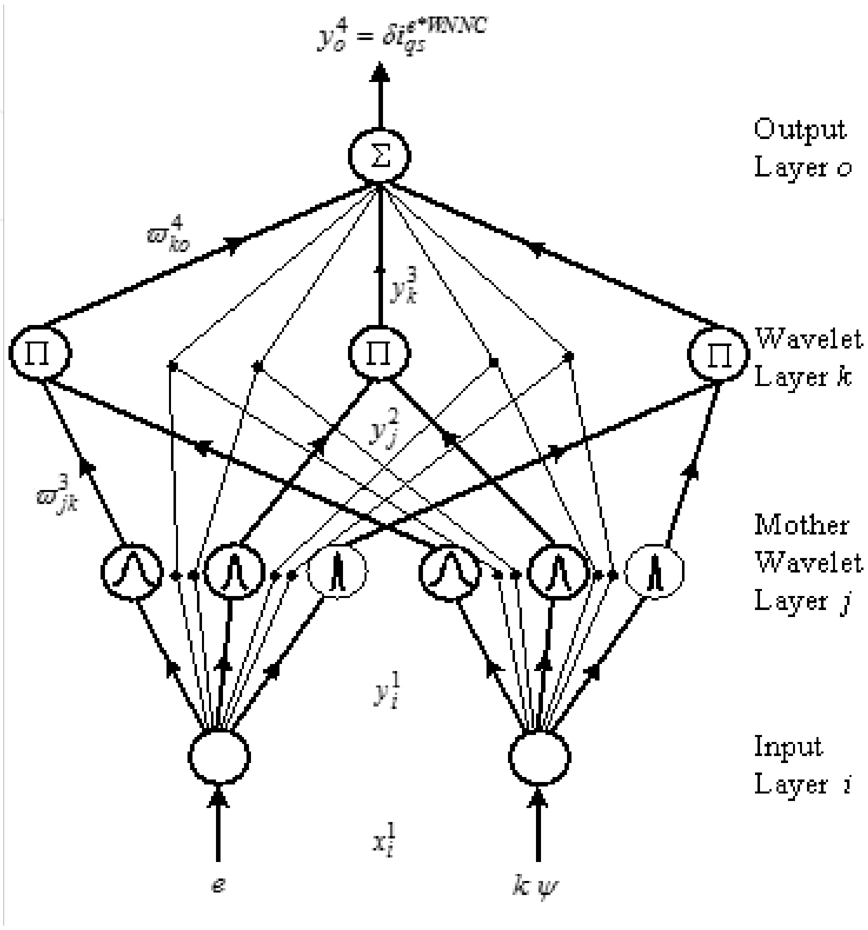

Figure 10. Four-layer wavelet–neural–network (WNN) structure.

The weight is updated by the amount:

$$\Delta\varpi_{ko}^4 = -\eta_v\frac{\partial E}{\partial \varpi_{ko}^4} = \left[-\eta_v\frac{\partial E}{\partial y_o^4}\cdot\frac{\partial y_o^4}{\partial net_o^4}\right]\cdot\frac{\partial net_o^4}{\partial \varpi_{ko}^4} = \eta_v\delta_o^4 x_k^4 \qquad (82)$$

where η_v is the learning rate parameter of the connecting weights of the output layer of the WNNC and will be optimized by the IPSO.

The weights of the output layer (layer 4) are updated according to the following equation.

$$\varpi_{ko}^4(N+1) = \varpi_{ko}^4(N) + \Delta\varpi_{ko}^4 = \varpi_{ko}^4(N) + \eta_v\delta_o^4 x_k^4 \qquad (83)$$

where N denotes the number of iterations.

In wavelet layer (layer 3), only the error term needs to be computed and propagated because the weights in this layer are unity.

$$\delta_k^3 = -\frac{\partial E}{\partial net_k^3} = \left(-\frac{\partial E}{\partial y_o^4}\cdot\frac{\partial y_o^4}{\partial net_o^4}\right)\cdot\left(\frac{\partial net_o^4}{\partial y_k^3}\cdot\frac{\partial y_k^3}{\partial net_k^3}\right) = \delta_o^4\omega_{ko}^4 \tag{84}$$

In the mother wavelet layer (layer 2), the multiplication operation is done. The error term is calculated as follows:

$$\delta_j^2 = -\frac{\partial E}{\partial net_j^2} = \left(-\frac{\partial E}{\partial y_o^4}\cdot\frac{\partial y_o^4}{\partial net_o^4}\cdot\frac{\partial net_o^4}{\partial y_k^3}\cdot\frac{\partial y_k^3}{\partial net_k^3}\right)\cdot\left(\frac{\partial net_k^3}{\partial y_j^2}\cdot\frac{\partial y_j^2}{\partial net_j^2}\right) = \sum_k \delta_k^3 y_k^3 \tag{85}$$

The update law of μ_{ij} is given by:

$$\Delta\mu_{ij} = -\eta_\mu\frac{\partial E_v}{\partial\mu_{ij}} = \left[-\eta_\mu\frac{\partial E}{\partial y_j^2}\cdot\frac{\partial y_j^2}{\partial net_j^2}\cdot\frac{\partial net_j^2}{\partial\mu_{ij}}\right] = \eta_\mu\delta_j^2\frac{2(x_i^2-\mu_{ij})^2}{(\sigma_{ij})^2} \tag{86}$$

The update law of σ_{ij} is given by:

$$\Delta\sigma_{ij} = -\eta_\sigma\frac{\partial E_v}{\partial\mu_{ij}} = \left[-\eta_\sigma\frac{\partial E}{\partial y_j^2}\cdot\frac{\partial y_j^2}{\partial net_j^2}\cdot\frac{\partial net_j^2}{\partial\sigma_{ij}}\right] = \eta_\sigma\delta_j^2\frac{2(x_i^2-\mu_{ij})^2}{(\sigma_{ij})^2} \tag{87}$$

where η_μ and η_σ are the learning rate parameters of the translation and dilation of the mother wavelet which will be optimized by the IPSO. The translation and dilation of the mother wavelet are updated as follows:

$$\mu_{ij}(N+1) = \mu_{ij}(N) + \Delta\mu_{ij} \tag{88}$$

$$\sigma_{ij}(N+1) = \sigma_{ij}(N) + \Delta\sigma_{ij} \tag{89}$$

To overcome the problem of uncertainties of the wind generation system due to parameter variations and to increase the on-line learning rate of the network parameters, a control law is proposed as follows.

$$\delta_o^4 = e + k\psi \tag{90}$$

Moreover, the selection of the values for the learning rates η_v, η_μ and η_σ has a significant effect on the network performance. In order to train the WNN effectively, three varied learning rates, which guarantee convergence of the tracking error based on the analyses of a discrete-type Lyapunov function, are adopted. The convergence analyses of the learning rates for assuring convergence of the tracking error is similar to [14] and is omitted here.

8.5. Improved Particle Swarm Optimization (IPSO)

In the PSO system, each particle adjusts its position according to its own experience and the experiences of neighbors, including the current velocity, position, and the best previous position experienced by itself and its neighbors. However, the efficiency of the PSO algorithm is affected by the randomly generated initial state. Therefore, the inertia weight Θ is adopted in the IPSO to balance between the local search ability and global search ability. Moreover, the inclusion of the worst experience component in the behavior of the particle in the IPSO gives additional exploration capacity to the swarm. Since the particle is made to remember its worst experience, it can explore the search space effectively to identify the promising solution region in [24]. Thus, the algorithm of the IPSO is derived as follows:

$$\begin{aligned} v_i^d(k+1) &= \Theta v_i^d(k) + c_1 \times r_1 \times (Pbest_i^d - x_i^d(k)) \\ &+ c_2 \times r_2 \times (Gbest_i^d - x_i^d(k)) + c_3 \times r_3 \times (Pworst_i^d - x_i^d(k)) \end{aligned} \tag{91}$$

$$x_i^d(k+1) = x_i^d(k) + v_i^d(k+1) \tag{92}$$

where $v_i^d(k)$ is the current velocity of ith particle, $i = 1,\dots, P$, in which P is the population size; the superscript d is the dimension of the particle; $Pbest_i^d$ is the best previous position of the ith particle; $Pworst_i^d$ is the worst previous position of the ith particle; $Gbest_i^d$ is the best previous position among all the particles in the swarm; $x_i^d(k)$ is the current position of the ith particle; c_1, c_2, and c_3 are the acceleration factors; and r_1, r_2 and r_3 represent the uniform random numbers between zero and one. In addition, the inertia weight Θ is set according to the following equation in [27]:

$$\Theta = \Theta_{\max} - \frac{\Theta_{\max} - \Theta_{\min}}{k_{\max}} \times k_n \tag{93}$$

where $k_{\max}$ is the maximum number of iterations and k_n is the current number of iteration. Equation (92) restricts the value Θ to the range $[\Theta_{\max}, \Theta_{\min}]$. In this Chapter, the maximum and minimum values of the inertia weights are $\Theta_{\max} = 0.7$ and $\Theta_{\min} = 0.4$, respectively.

8.6. WNN Learning Rates Tuning Using IPSO

To further improve the online learning capability of the proposed WNN, the IPSO algorithm is adopted in this Chapter to adapt the learning rates η_v^v , η_μ^v , η_σ^v , η_v^P , η_μ^P , η_σ^P , η_v^Q , η_μ^Q and η_σ^Q in the backpropagation learning methodology of the WNN. Moreover, the procedure of the IPSO algorithm is shown in Figure 11 and is described as follows.

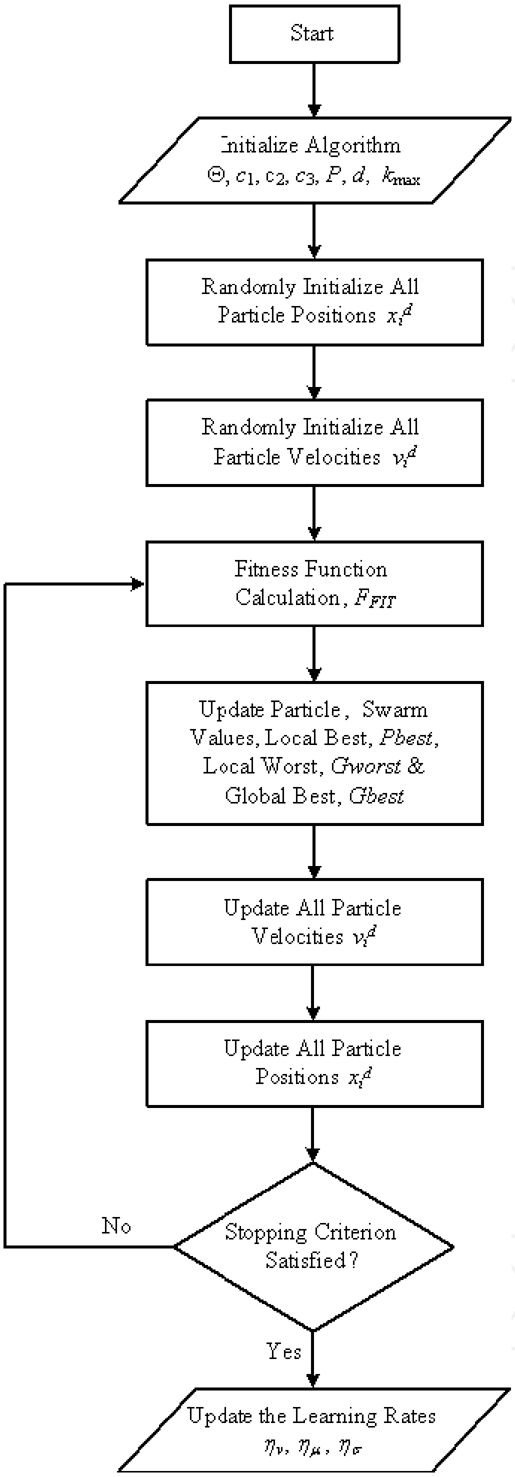

Figure 11. Flowchart implementation of the IPSO algorithm.

1) Initialization: Randomly generate the initial trial vectors $x_i^d(k)$, which indicate the possible solutions for the learning rates. Moreover, the population size is set to P = 15, and the dimension of the particle is set to d = 9 in this Chapter. This step is accomplished by setting $x_i^d = [x_i^0, x_i^1, x_i^2, x_i^3, x_i^4, x_i^5, x_i^6, x_i^7, x_i^8]$ represent the desired values of the learning rates η_v^v,

η_μ^v , η_σ^v , η_v^P , η_μ^P , η_σ^P , η_v^Q , η_μ^Q and η_σ^Q , respectively. Furthermore, the elements in vector x_i^d are randomly generated as follows:

$$x_i^d \sim U[\eta_{\min}^d, \eta_{\max}^d] \tag{94}$$

where $U[\eta_{\min}^d, \eta_{\max}^d]$ designates the outcome of a uniformly distributed random variable ranging over the given lower- and upper-bounded values $\eta_{\min}$ and $\eta_{\max}$ of the learning rate.

2) Determination of fitness function: For each trial vector x_i^d , a fitness value should be assigned and evaluated. In this project, a suitable fitness function is selected to calculate the fitness value and defined as

$$F_{FIT} = \frac{1}{0.1 + abs(V_{dc}^* - V_{dc}) + abs(P^* - P) + abs(Q^* - Q)} \tag{95}$$

where F_{FIT} is the fitness value and *abs*() is the absolute function; 0.1 is added in the dominant part to avoid the fitness value approaching infinite when the error of the DC-link voltage approaches zero.

3) Selection and memorization: Each particle x_i^d memorizes its own fitness value and chooses the maximum one that is the best so far as $Pbest_i^d$, and the maximum vector in the population $Pbest = [Pbset_1^d, Pbest_2^d, \ldots, Pbest_p^d]$ is obtained. Moreover, each particle x_i^d is set directly to $Pbest_i^d$ in the first iteration, and the particle with the best fitness value among *Pbest* is set to be the global best $Gbest^d$.

4) Modification of velocity and position: The modification of each particle is based on (90, 91).

5) Stopping rule: Repeat steps (1)–(4) until the best fitness value for *Gbest* is obviously improved or a set count of the generation is reached. The solution with the highest fitness value is chosen as the best learning rates of the WNN. By using the online tuning learning rates based on IPSO, the WNNC can regulate the DC-link voltage of the CRPWM AC/DC converter, active and reactive power of the CRPWM DC/AC inverter effectively.

In the IPSO, since the global best $Gbest^d$ has higher priority than the local best $Pbest_i^d$ and local worst in the optimal algorithm, the acceleration factors are chosen to be $c_1 = c_2 = 0.6$ and $c_3 = 3.10$. Moreover, to achieve better global search ability for the IPSO, larger movement is required for the particle with the chosen larger inertia weight w in the beginning of the optimization process. Then, a smaller inertia weight Θ is required to improve the searching accuracy after several times of optimization. Furthermore, the inertia weight Θ must be less than one to avoid the divergence of the particle. Therefore, the maximum and minimum values of the inertia weights are chosen to be $\Theta_{\max} = 0.7$ and $\Theta_{\min} = 0.4$, respectively.

9. Numerical Simulation Results

In this section, a computer simulation results for the proposed wind generation system are provided to demonstrate the effectiveness of the proposed control schemes. The wind turbine SEIG system simulation is carried out using MATLAB/SIMULINK package. Since this Chapter is dealing with an isolated wind energy conversion system with maximum power control, the more realistic approach for an isolated wind power control system is to choose the DC-link voltage, active power and reactive power as the controlled variables.

Wind Speed	Tip Speed Ratio λ	Power Coefficient C_P	Reference Rotor Speed of WTE	Wind Turbine Output Power P_m (W)	IG Output Power P_{IG} (W)	DC-Link Power P_{DC} (W)
V_w=16 m/sec	6.7	0.37	≈ 296 rad/sec	≈ 1580	≈ 1500	≈ 1400
V_w=14 m/sec	6.7	0.37	≈ 259 rad/sec	≈ 1086	≈ 1030	≈ 965
V_w=12 m/sec	6.7	0.37	≈ 222 rad/sec	≈ 705	≈ 670	≈ 637
V_w=10 m/sec	6.7	0.37	≈ 185 rad/sec	≈ 422	≈ 400	≈ 392
V_w=8 m/sec	6.7	0.37	≈ 148 rad/sec	≈235	≈ 223	≈ 212
V_w=6 m/sec	6.7	0.37	≈ 111 rad/sec	≈ 110	≈ 104	≈ 95

Table 1. Parameters of the wind turbine emulator (WTE) at various wind speeds.

Therefore, the DC-link voltage control, active power control and reactive power control using the PID controllers and WNNCs with IPSO are carried out for comparison. The dynamic performance of the wind generation system using double-sided CRPWM AC/DC/AC power converter system connected to utility grid subjected to three different wind speed variation profiles are shown in Figures (12-16). The first wind speed variation profile is the stepwise, the second is the sinusoidal variation profile and the last is the trapezoidal variation profile as given in the following section. The performance of the whole system at six operating conditions of wind speeds 6, 8, 10, 12, 14 and 16 m/sec is studied as shown in Table 1. The corresponding reference rotor speeds of the IG are 111, 148, 185, 222, 259 and 296 rad/sec, respectively. The respective wind turbine output power, DC-link power commands and IG output power are also shown in Table 1.

9.1. Wind Generation System Performance with CRPWM AC/DC/AC Converters Using Stepwise Wind Speed Profile

The dynamic response of the wind generation system feeding the double-sided CRPWM AC/DC/AC power converter connected to utility grid based on the maximum power point tracking (MPPT) control scheme using stepwise profile for wind speed variations of 10 m/s, 12 m/s, 14 m/s and 16 m/s are shown in Figures 12 and 13 utilizing both PID controller and WNNC with IPSO. These responses are the wind speed, rotor speed of the IG, the q-axis torque control current of the IG, the DC-link voltage V_{dc}, the DC-link power P_{dc} and the DC-link current i_{dc}, respectively, for the CRPWM converter fed from the SEIG. Furthermore, the maximum active and reactive power injected to the grid at unity power factor, d-q axis currents, the phase voltage and currents, respectively, at the AC side of the CRPWM inverter connected to the utility grid. The dynamic responses of the wind speed, rotor speed of the IG, the q-axis torque control current of the IG, the DC-link voltage V_{dc}, the DC-link power P_{dc} and the DC-link current i_{dc}, respectively, are shown in Figure (12-X) for both PID and WNNC with IPSO controllers for the CRPWM converter fed from the IG. In this simulation, the wind speed is changed from 10 m/s to 12 m/s, then changed back from 12 m/s to 10 m/s and the reference voltage for the DC-link is changed from 0 to 539 V. From the simulation results shown in Figure 12-Xa, sluggish DC-link voltage tracking response is obtained for the PID controller owing to the weak robustness of the linear controller. Moreover, approximately 2 sec is required for the PID-controlled SEIG system to generate the maximum output power. In addition, from the simulation results, fast dynamic response for the DC-link voltage can be obtained for the hybrid control of the SEIG wind generation system owing to the on-line training of the WNNC with IPSO. Moreover, the robust control performance of the proposed hybrid control system using the WNNC with IPSO at different operating conditions is obvious. Furthermore, approximately 1 sec is required for the SEIG to generate the maximum output power. In addition, the dynamic response of the wind generation system using the hybrid control scheme with the WNNC using IPSO is much better as shown in Figure 12-Xb. As a result, comparing the results of PID controller with the WNNC, the proposed hybrid voltage controller is more suitable to control the DC-link voltage of the CRPWM converter-based SEIG wind generation system under the possible occurrence of load disturbance and parameter variations.

The output voltage of the DC-link is fed to the CRPWM inverter connected to the utility grid. The dynamic response of the CRPWM inverter system feeding the utility grid using PID controllers and WNNC with IPSO for active and reactive power control at the same condition of wind speed variations and the DC-link voltage command is shown in Figure 12-Y with MPPT control scheme. These responses are the maximum active and reactive power, d-q axis currents of the CRPWM inverter, the grid voltages and currents at the AC side of the CRPWM inverter, respectively. It is obvious that zero reactive power and zero d-axis current which confirms unity power factor operation at different wind speeds. At the same time the q-axis current and the active power follow their references to give the MPPT. From the simulation results shown in Figure 12-Ya, sluggish active power tracking response is obtained for the PID controller owing to the weak robustness of the linear controller. Moreover, approximately 1.6 sec is required for the PID-controlled CRPWM inverter system to track the maximum power. In addition, from the simulation results, fast dynamic response for the active power can be obtained for the hybrid control of the CRPWM inverter system owing to the on-line training of the WNNC with IPSO. Moreover, the robust control performance of the proposed hybrid control system using the WNNC with IPSO at different operating conditions is obvious. Furthermore, approximately 0.8 sec is required for the CRPWM inverter system to track the maximum power. In addition, the dynamic response of the CRPWM inverter system connected to the utility grid using the hybrid control scheme with the WNNC with IPSO is much better as shown in Figure 12-Yb. As a result, comparing the results of PID with the WNNC-based IPSO, the proposed hybrid active and reactive power controllers are more suitable to control the power of the CRPWM converter/inverter system connected to the utility grid under the possible occurrence of parameter variations. Additionally, from these figures, it is evident that a unity power factor operation is achieved at different wind speeds. Furthermore, it is obvious that the proposed control scheme illustrates satisfactory performance and good tracking characteristics.

To confirm the effectiveness of the proposed control schemes, the wind speed is changed from 14 m/s to 16 m/s, then changed back from 16 m/s to 14 m/s. The dynamic response of the wind generation system using double-sided CRPWM AC/DC/AC power converters is shown in Figure 13. As result, comparing the results of PID controllers and the WNNCs with IPSO, the proposed hybrid controller gives robust performance for both the DC-link voltage, active and reactive power of the AC/DC/AC CRPWM converter considering the existence of parameter variations and load disturbances for the wind generation system.

9.2. Wind Generation System Performance with CRPWM AC/DC/AC Converters Using Sinusoidal Wind Speed Profile

In order to investigate the effectiveness of the proposed control schemes, the sinusoidal profile for wind speed variations. The dynamic response of the wind generation system using double-sided CRPWM AC/DC/AC power converters using both PID controllers and WNNCs with IPSO technique for the DC-link voltage, active and reactive power is shown in Figure 14. It is obvious from Figure 14 that good dynamic performance is achieved and the DC-link actual voltage, actual active and reactive power follow their references. In addition, the dynamic performance of the wind generation system using the hybrid control scheme with the WNNCs utilizing IPSO is much better as shown in Figure 14 and provide robust performance considering the existence of parameter variations and load disturbances for the wind generation system.

9.3. Wind Generation System Performance with CRPWM AC/DC/AC Converters Using Trapezoidal Wind Speed Profile

The wind generation system is re-subjected to trapezoidal profile for the wind speed variations to study the effectiveness of the proposed control schemes. The dynamic response of the wind generation system using double-sided CRPWM AC/DC/AC power converters using both PID controllers and WNNCs with IPSO technique for the DC-link voltage, active and reactive power is shown in Figure 15.

It is obvious that good dynamic performance is achieved and the DC-link actual voltage, actual active and reactive power follow their references. The line current and voltage at the AC side of the CRPWM inverter at different wind speeds showing unity power factor operation are shown in Figure 16. As a result, comparing the results of PID controller with the hybrid control scheme with the WNNC-based IPSO, the proposed hybrid controllers are more suitable to control the voltage and power of the CRPWM converter/inverter system connected to the utility grid under the possible occurrence of parameters variations. Additionally, it is evident that unity power factor operation is achieved at different wind speed profiles. It is clear that the proposed control scheme illustrates satisfactory performance and good tracking characteristics.

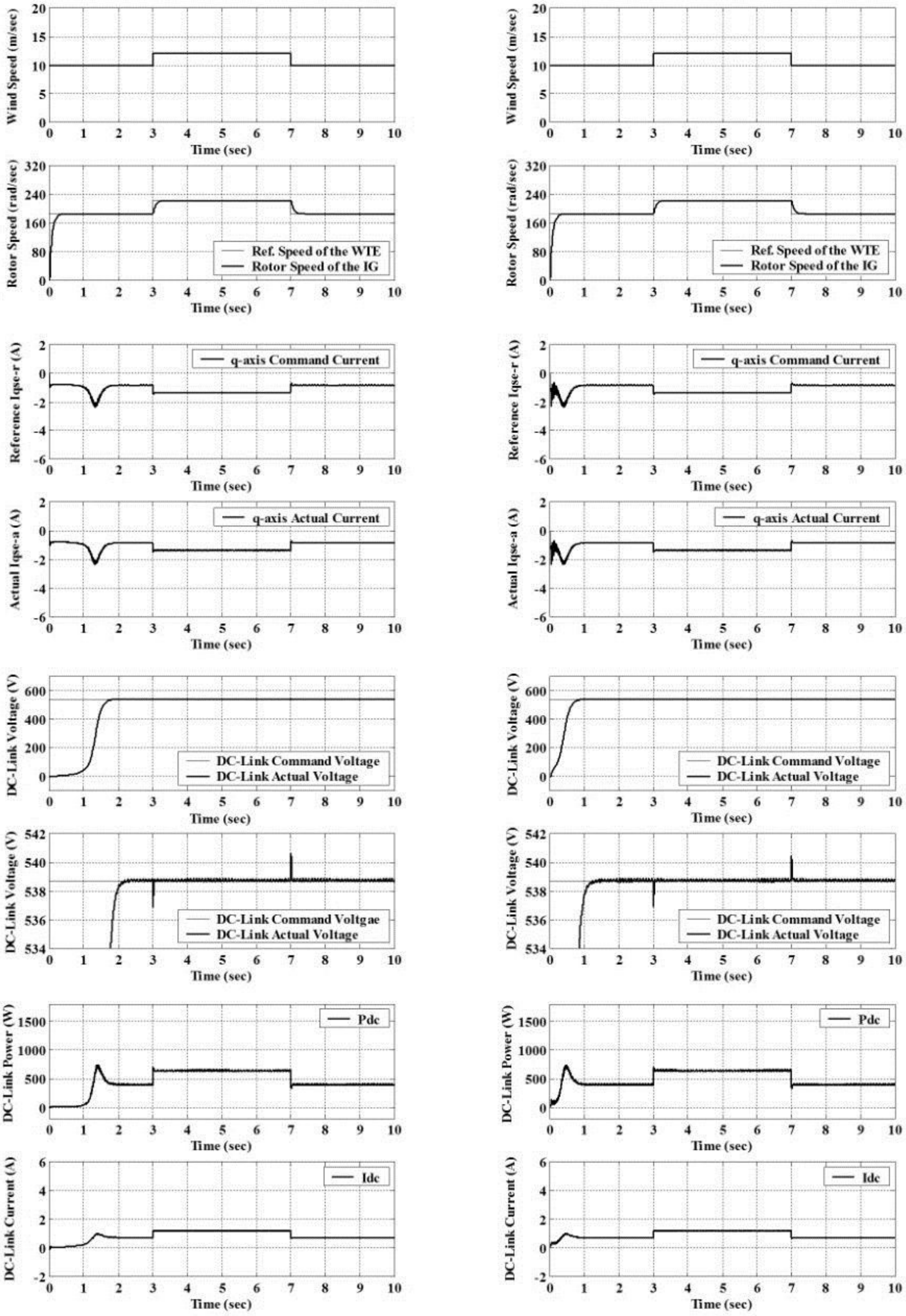

(a) (b)

(X) Dynamic response of the DC-link voltage controlled SEIG system

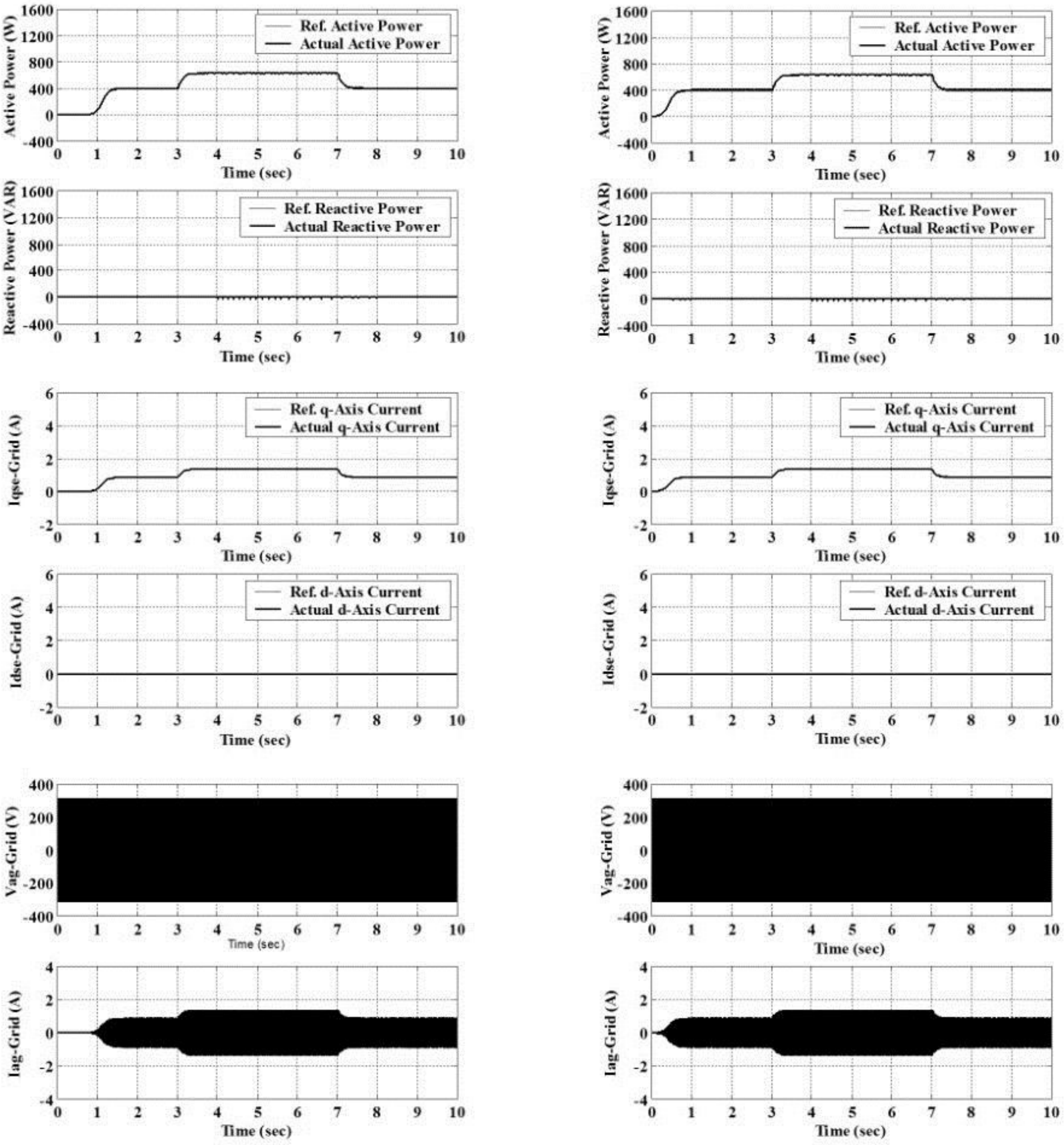

(a) (b)

(Y) Dynamic response of the CRPWM inverter connected to the utility grid

Figure 12. Dynamic performance of the wind generation system using stepwise profile wind speed changed from V_w =10 m/sec to V_w =12 m/sec to V_w =10 m/sec. (a) Using PID controller (b) Using WNNC with IPSO.

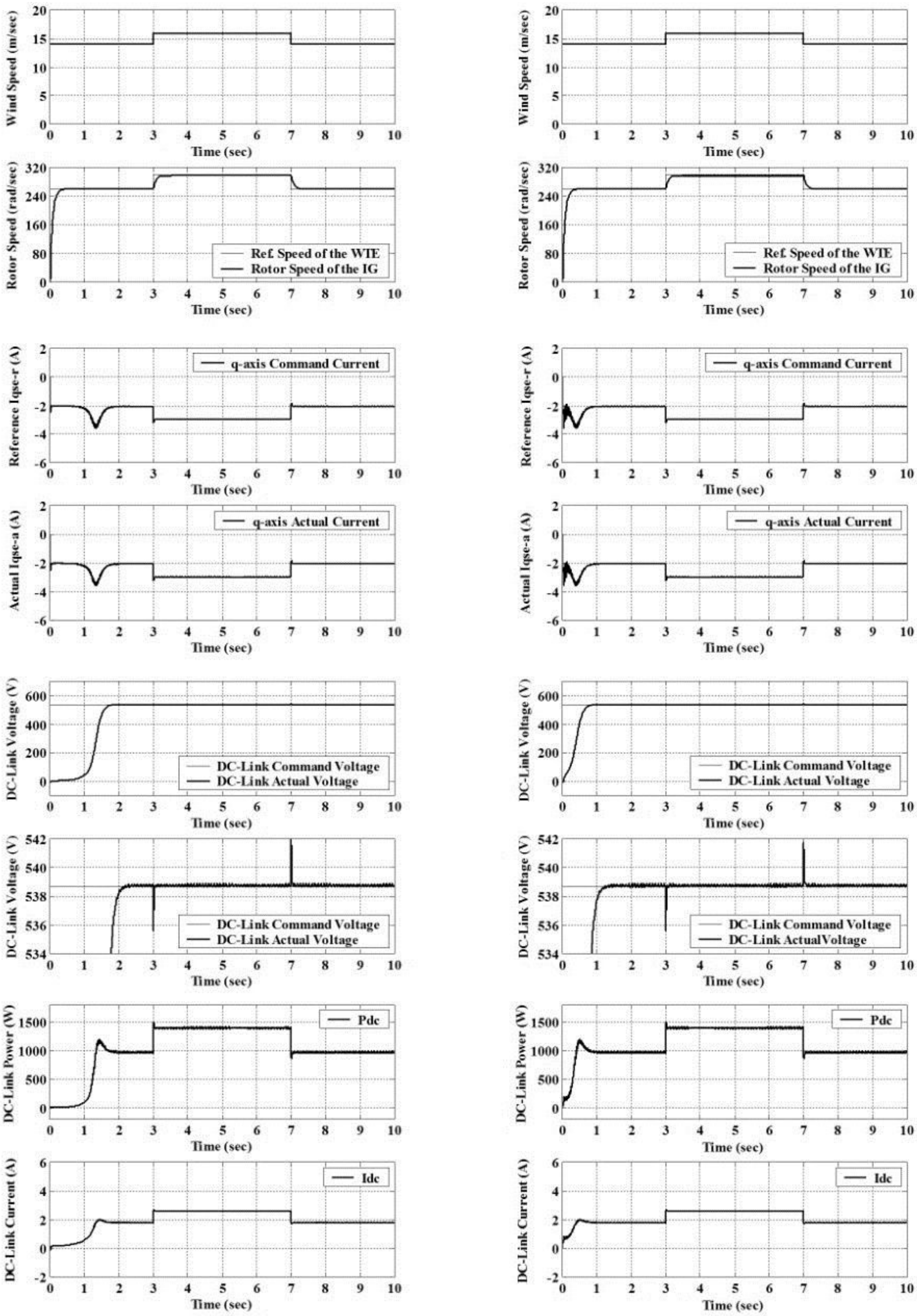

(a)

(b)

(X) Dynamic response of the DC-link voltage controlled SEIG system

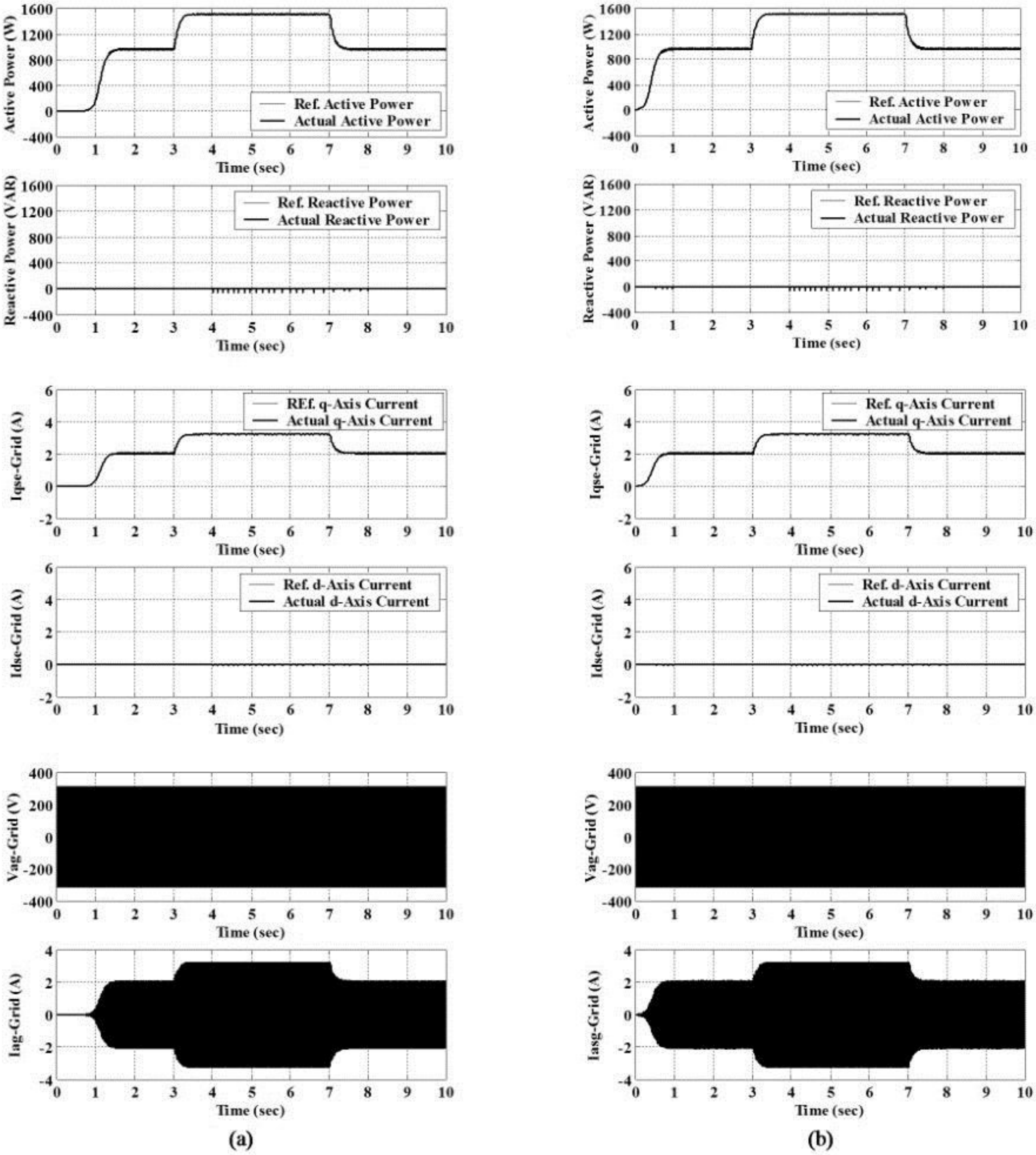

(Y) Dynamic response of the CRPWM inverter connected to the utility grid

Figure 13. Dynamic performance of the wind generation system using stepwise profile wind speed changed from V_w =14 m/sec to V_w =16 m/sec to V_w =14 m/sec. (a) Using PID controller (b) Using WNNC with IPSO.

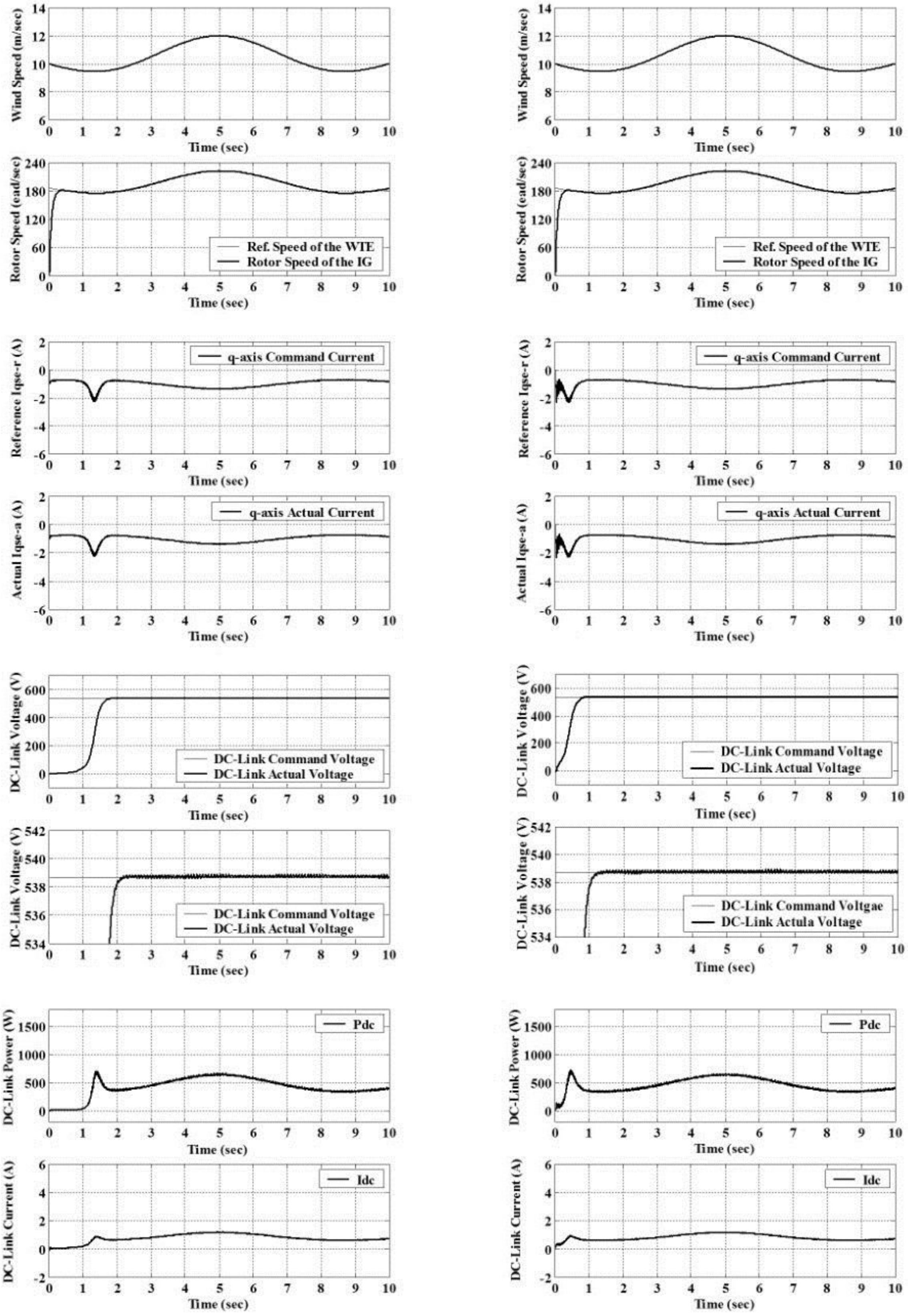

(a) (b)

(X) Dynamic response of the DC-link voltage controlled SEIG system

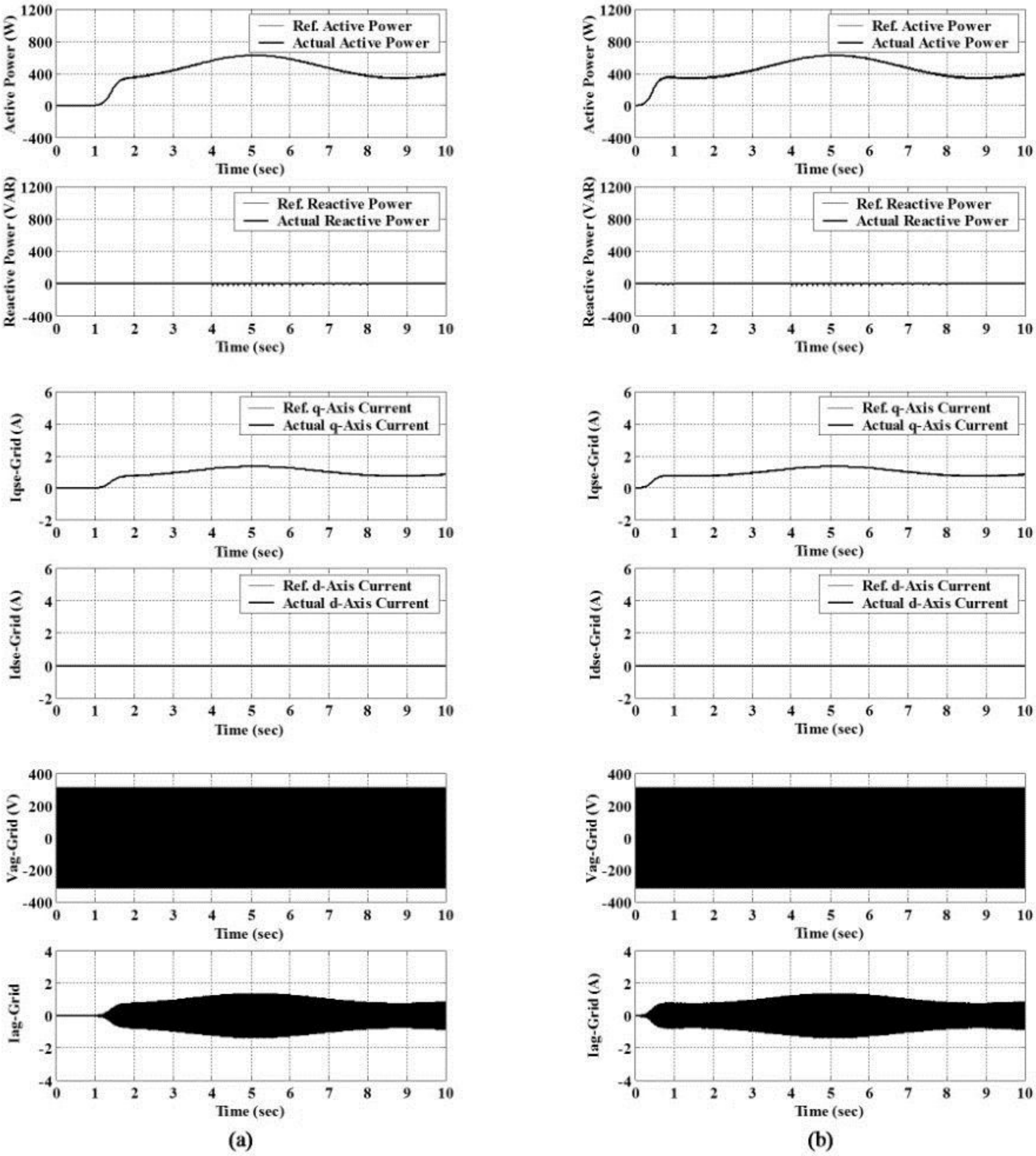

(Y) Dynamic response of the CRPWM inverter connected to the utility grid

Figure 14. Dynamic performance of the wind generation system using sinusoidal profile wind speed variations. (a) Using PID controller (b) Using WNNC with IPSO.

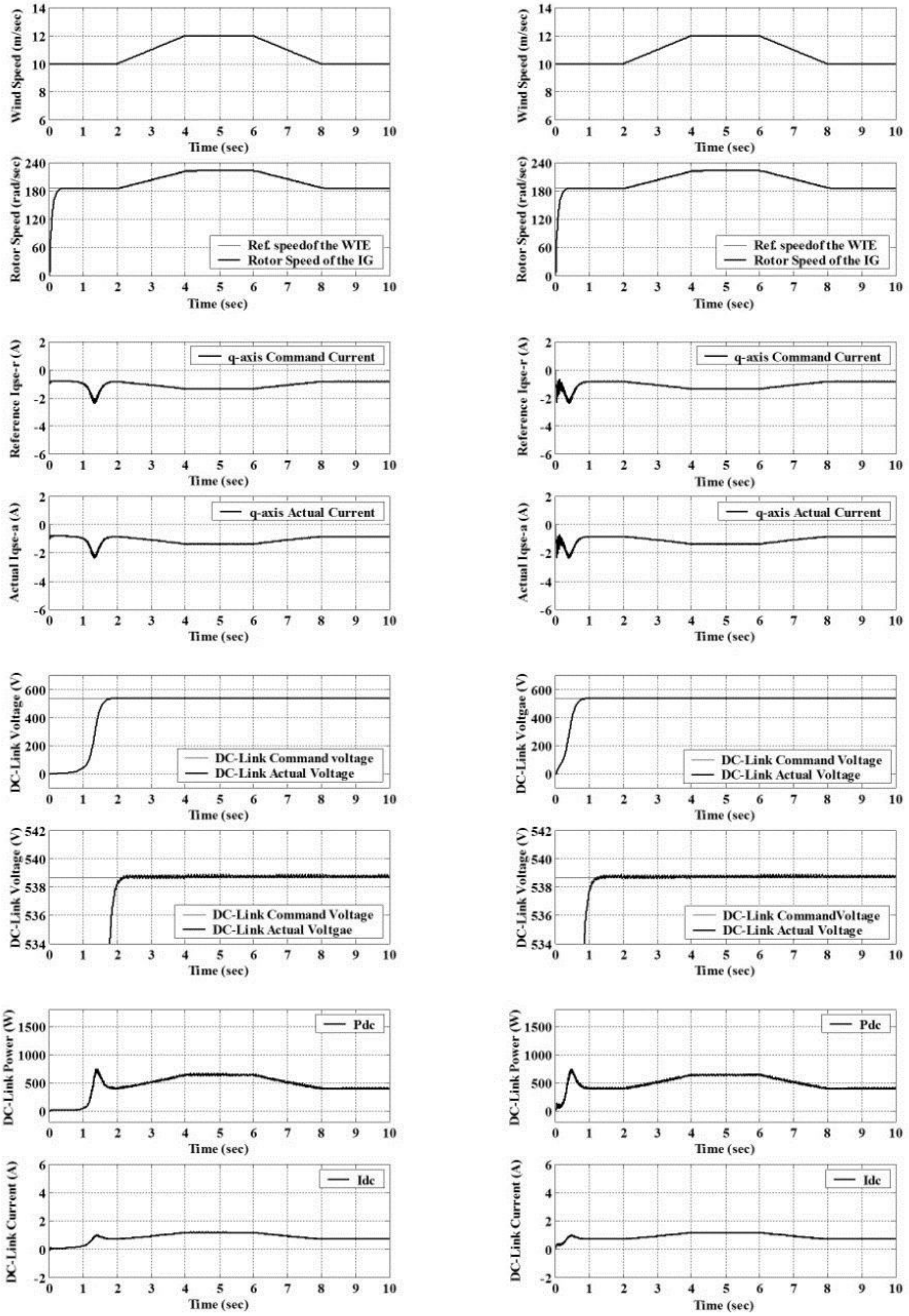

(a) (b)

(X) Dynamic response of the DC-link voltage controlled SEIG system

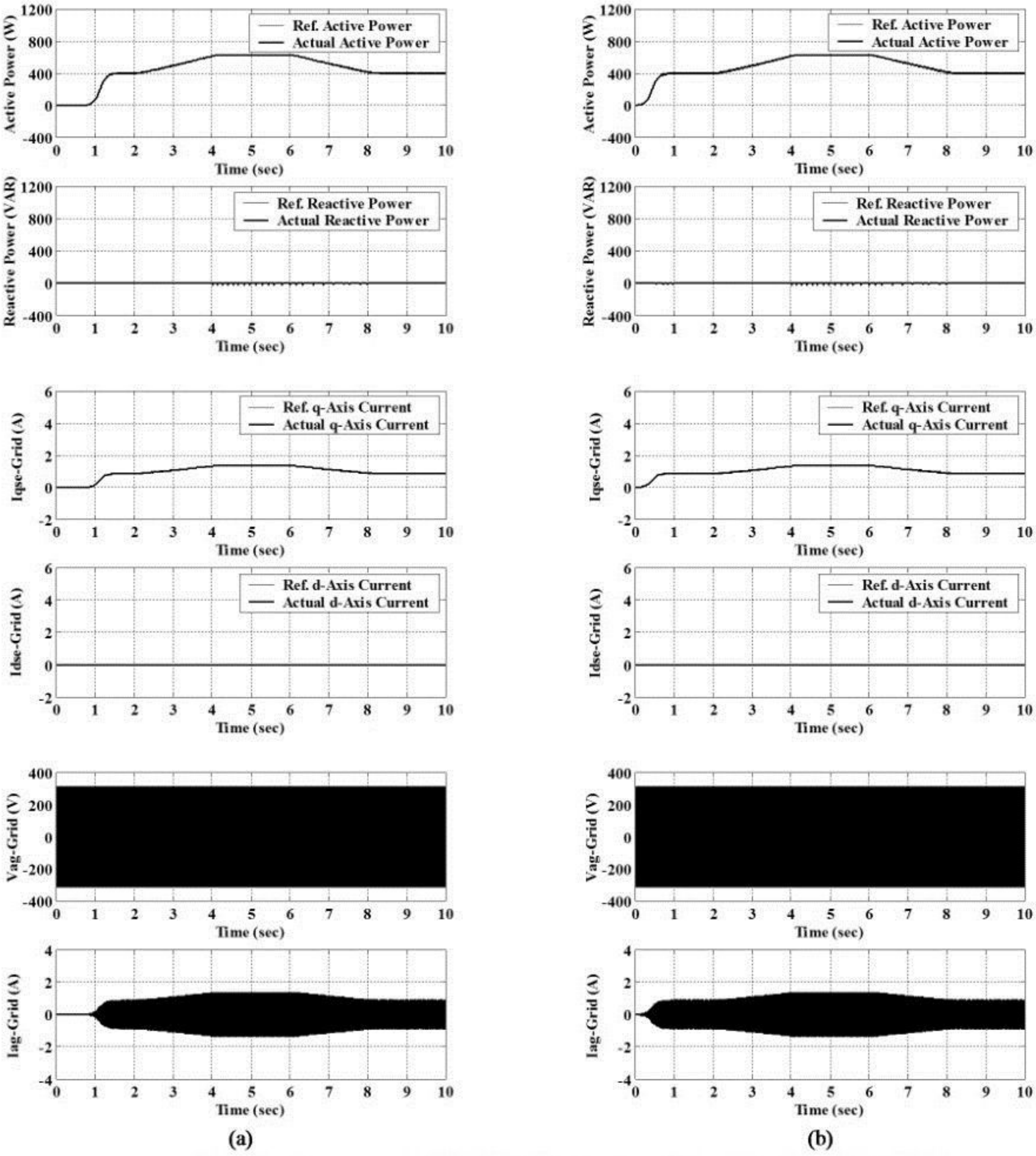

(Y) Dynamic response of the CRPWM inverter connected to the utility grid

Figure 15. Dynamic performance of the wind generation system using trapezoidal profile wind speed variations. (a) Using PID controller (b) Using WNNC with IPSO.

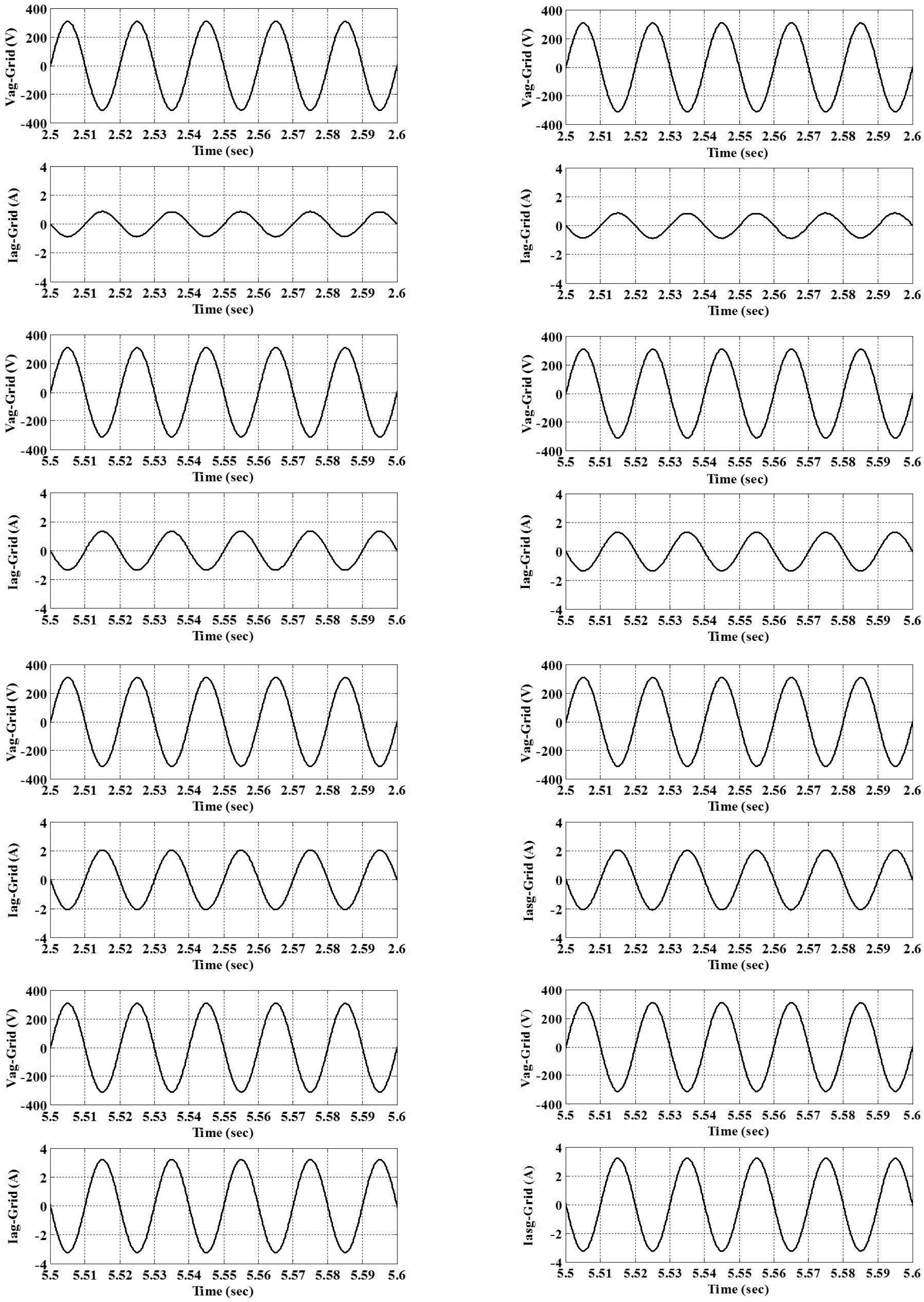

(a) (b)

Figure 16. Line side voltage and current showing unity power factor operation at different wind speeds V_w =10 m/sec, V_w =12 m/sec, V_w =14 m/sec and V_w =16 m/sec from top to bottom (a) Using PID controller (b) Using WNNC with IPSO

10. Conclusion

This Chapter proposed a hybrid control scheme utilizing WNNCs with IPSO for the voltage control of DC-link voltage, active power and reactive power of the CRPWM AC/DC/AC power converter feeding from a wind turbine SEIG system. The double-sided AC/DC/AC CRPWM converter is connected to the utility grid and operated under IFOC and VFOC which guarantees the robustness in the presence of parameter uncertainties and load disturbances. The IG is controlled by the maximum power point tracking (MPPT) control technique below the base speed and the maximum energy can be captured from the wind turbine. The proposed hybrid controller consists of a three feed-back PID controller in addition to a three on-line trained WNNC with IPSO. Also, this Chapter successfully demonstrated the application of the PID control and WNN control systems to control the voltage of the DC-link, active power and reactive power of the CRPWM AC/DC/AC power converter. Therefore, the DC-link voltage tracking response, active power and reactive power can be controlled to follow the response of the reference commands under a wide range of operating conditions. Simulation results have shown that the proposed hybrid control scheme using the WNNC with IPSO grants robust tracking response and good regulation characteristics in the presence of parameter uncertainties and external load disturbances. Moreover, simulations were carried out at different wind speeds to testify the effectiveness of the proposed hybrid controller. Finally, the main contributions of this Chapter are the successful development of the hybrid control system, in which a WNNC with IPSO is utilized to compensate the uncertainty bound in the wind generation system on-line and the successful application of the proposed hybrid control scheme methodology to control the DC-link voltage, active and reactive power of the AC/DC/AC CRPWM converter considering the existence of parameters uncertainties and external load disturbances.

Author details

Fayez F. M. El-Sousy[1] and Awad Kh. Al-Asmari[2*]

*Address all correspondence to: alasmari@ksu.edu.sa

1 College of Engineering, Department of Electrical Engineering Salman bin Abdulaziz University, Al-Kharj, Saudi Arabia

2 College of Engineering, King Saud University, Riyadh, and Vice Rector for Graduate Studies and Research, Salman bin Abdulaziz University, Saudi Arabia

References

[1] Zinger, D. S., & Muljadi, E. (1997). Annualized Wind Energy Improvement Using Variable Speeds. *IEEE Trans. on Industry Applications*, 33(6), 1444-1447.

[2] Seyoum, D., Grantham, C., & Rahman, M. F. (2003). The Dynamic Characteristics of an Isolated Self-Excited Induction Generator Driven by a Wind Turbine. *IEEE Trans. on Industry Applications*, 39(4), 936-944.

[3] Malik, N. H., & Al-Bahrani, A. H. (1990). Influence of the Terminal Capacitor on the Performance of a Self-Excited Induction Generator. *IEE Proc.*, 137(2), 168-173.

[4] Wang, L., & Ching-Huei, L. (1997). A Novel Analysis on the Performance of an Isolated Self-Excited Induction Generator. *IEEE Trans. on Energy Conversion*, 12(2), 109-117.

[5] Dixon, J. W., & Ooi, B. T. (1998). Indirect Current Control of a Unity Power Factor Sinusoidal Boost Type 3-Phase Rectifier. *IEEE Trans. on Industrial Electronics*, 35(4), 508-515.

[6] Sugimoto, H., Moritomo, S., & Yano, M. (1988, 11-14 April 1988). A High Performance Control Method of a Voltage-Type PWM Converter. Kyoto, Japan. *Proceedings of the19th Annual IEEE Power Electronics Specialists Conference, PESC*, 360-368.

[7] Datta, R., & Ranganathan, V. T. (2003). A Method of Tracking the Peak Power Points for a Variable Wind Energy Conversion System. *IEEE Trans. on Energy Conv.*, 18(1), 163-168.

[8] Martinez, F., Gonzalez, J. M., Vazquez, J. A., & De Lucas, L. C. (2002, 5-8 Nov.) Sensorless Control of a Squirrel Cage Induction Generator to Track the Peak Power in a Wind Turbine. *Proceedings of the 28th Annual IEEE Conference of the Industrial Electronics Society IEEE-IECON*, 169-174.

[9] Simoes, M. G., & Bose, B. K. (1997). Design and Performance Evaluation of a Fuzzy-Logic-Based Variable-Speed Wind Generation System. *IEEE Trans. Industry Appli.*, 33(4), 956-965.

[10] Cardenas, R., & Pena, R. (2004). Sensor-Less Vector Control of Induction Machine for Variable-Speed Wind Energy Applications. *IEEE-Trans. on Energy Conversion*, 19(1), 196-205.

[11] Seyoum, D., Rahman, M. F., & Grantham, C. (2003, 9-13 Feb.) Terminal Voltage Control of a Wind Turbine Driven Induction Generator Using Stator Oriented Field Control. *Proceedings of the Eighteenth Annual IEEE Applied Power Electronics Conference and Exposition, IEEE-APEC'03*, 846-852.

[12] El -Sousy, F. F. M., Orabi, M., & Godah, H. (2006). Maximum Power Point Tracking Control Scheme for Grid Connected Variable Speed Wind Driven Self-Excited Induction Generator. *Journal of Power Electronics (JPE)*, 6(1), 52-66.

[13] Lin, F. J., Huang, P. K., Wang, C. C., & Teng, L. T. (2007). An Induction Generator System Using Fuzzy Modeling and Recurrent Fuzzy Neural Network. *IEEE Trans. Power Electron.*, 22(1), 260-271.

[14] Lin, F. J., Teng, L. T., Shieh, P. H., & Li, Y. F. (2006). Intelligent Controlled Wind Turbine Emulator and Induction Generator System Using RBFN. *Proc. Inst. Elect. Eng.*, 153(4), 608, 618.

[15] Zhang, Q., & Benveniste, A. (1992). Wavelet Networks. *IEEE Trans. on Neural Networks*, 3(6), 889-898.

[16] Zhang, J., Walter, G. G., Miao, Y., & Lee, W. N. W. (1995). Wavelet Neural Networks for Function Learning. *IEEE Trans. on Signal Processing*, 43(6), 1485-1496.

[17] Zhang, Z., & Zhao, C. (2007, May 30 - June 1). A Fast Learning Algorithm for Wavelet Network and its Application in Control. China. *Proceedings of the IEEE International Conference on Control and Automation, IEEE ICCA*, 1403-1407.

[18] Sureshbabu, N., & Farrell, J. A. (1999). Wavelet-Based System Identification for Nonlinear Control. *IEEE Trans. on Automatic Control*, 44(2), 412-417.

[19] Billings, S. A., & Wei, H. L. (2005). A New Class of Wavelet Networks for Nonlinear System Identification. *IEEE Trans. on Neural Network*, 16(4), 862-874.

[20] Giaouris, D., Finch, J. W., Ferreira, O. C., Kennel, R. M., & El -Murr, G. M. (2008). Wavelet Denoising for Electric Drives. *IEEE Trans. on Industrial Electronics*, 55(2), 543-550.

[21] Hsu, C. F., Lin, C. M., & Lee, T. T. (2006). Wavelet Backstepping Control for a Class of Nonlinear Systems. *IEEE Transactions Neural Networks*, 17(5), 1175-83.

[22] Astrom, K. J., & Wittenmark, B. (1995). *Adaptive Control*, New York, Addison Wesley.

[23] Slotine, J.-J., & Li, W. (1991). *Applied Nonlinear Control*, Englewood Cliffs, NJ, Printice-Hall.

[24] Kennedy, J., & Eberhart, R. (1995, Nov. 27 - Dec. 1). Particle Swarm Optimization. Perth-Australia. *Proceedings of the IEEE International Conference on Neural Networks, IEEE-ICNN*, 1942-1948.

[25] Maurice, C. (2006). *Particle Swarm Optimization*, Paris, France, France Télécom.

[26] Jacob, R., & Yahya, R. S. (2004). Particle Swarm Optimization in Electromagnetics. *IEEE Trans. Antennas Propag.*, 52(2), 397-407.

[27] Gaing, Z. L. (2004). A Particle Swarm Optimization Approach for Optimum Design of PID Controller in AVR System. *IEEE Trans. Energy Conv.*, 19(2), 384-391.

[28] Juang, C. F., & Hsu, C. H. (2005). Temperature Control by Chip-Implemented Adaptive Recurrent Fuzzy Controller Designed by Evolutionary Algorithm. *IEEE Trans. Circuits Syst. I*, 52(11), 2376-2384.

[29] Parrott, D., & Li, X. (2006). Locating and Tracking Multiple Dynamic Optima by a Particle Swarm Model Using Speciation. *IEEE Trans. Evolutionary Computat.*, 10(4), 440-458.

[30] Valle, Y., Venayagamoorthy, G. K., Mohagheghi, S., Hernandez, J.-C., & Harley, R. G. (2008). Particle Swarm Optimization: Basic Concepts, Variants and Applications in Power Systems. *IEEE Trans. on Evolutionary Computation*, 12(2), 171-195.

[31] Eberhart, R. C., & Shi, Y. (1998, 4-9 May). Comparison Between Genetic Algorithm and Particle Swarm Optimization. Anchorage, AK USA. *Proceedings of the IEEE International Conference on Evolutionary. Computation*, 611-616.

[32] Angeline, P. J. (1998, 4-9May). Using Selection to Improve Particle Swarm Optimization. Anchorage, AK USA. *Proceedings of the IEEE International Conference on Evolutionary. Computation*, 84-98.

[33] Yoshida, H., Kawata, K., & Fukuyama, Y. (2000). A Particle Swarm Optimization for Reactive Power and Voltage Control Considering Security Assessment. *IEEE Trans. on Power Systems*, 15(4), 1232-1239.

[34] Teng, L. T., Lin, F. J., Chiang, H. C., & Lin, J. W. (2009). Recurrent Wavelet Neural Network Controller with Improved Particle Swarm Optimisation for Induction Generator System. *IET Electr. Power Appl.*, 3(2), 147-159.

[35] Marra, E. G., & Pomillio, J. A. (2000). Induction-Generator-Based System Providing Regulated Voltage with Constant Frequency. *IEEE Trans. Ind. Electron.*, 47(4), 908-914.

[36] Ojo, O., & Davidson, I. E. (2000). PWM-VSI Inverter-Assisted Stand-Alone Dual Stator Winding Induction Generator. *IEEE Trans. Ind. Appl.*, 36(6), 1604-1611.

[37] Wekhande, S., & Agarwal, V. (2001). Simple Control for a Wind-Driven Induction Generator. *IEEE Ind. Appl. Mag.*, 7(2), 44-53.

[38] Portillo, R. C., Prats, M. M., Leon, J. I., Sanchez, J. A., Carrasco, J. M., Galvan, E., & Franquelo, L. G. (2006). Modeling Strategy for Back-to-Back Three-Level Converters Applied to High-Power Wind Turbines. *IEEE Trans. Ind. Electron.*, 53(5), 1483-1491.

[39] Chatterjee, J. K., Perumal, B. V., & Gopu, N. R. (2007). Analysis of Operation of a Self-Excited Induction Generator with Generalized Impedance Controller. *IEEE Trans. Energy Convers.*, 22(2), 307-315.

[40] Hilloowala, R. M., & Sharaf, A. M. (1996). A Rule-Based Fuzzy Logic Controller for a PWM Inverter in a Stand Alone Wind Energy Conversion Scheme. *IEEE Trans. Ind. Appl.*, 31(1), 57-65.

[41] Battista, H. D., Mantz, R. J., & Christiansen, C. F. (2000). Dynamical Sliding Mode Power Control of Wind Driven Induction Generators. *IEEE Trans. Energy Convers.*, 15(4), 451-457.

[42] Mirecki, A., Roboam, X., & Richardeau, F. (2007). Architecture Complexity and Energy Efficiency of Small Wind Turbines. *IEEE Trans. Ind. Electron.*, 54(1), 660-670.

[43] Kojabadi, H. M., Chang, L., & Boutot, T. (2004). Development of a Novel Wind Turbine Simulator for Wind Energy Conversion Systems Using an Inverter Controlled Induction Motor. *IEEE Trans. Energy Convers.*, 19(3), 547-552.

[44] Teodorescu, R., & Blaabjerg, F. (2004). Flexible Control of Small Wind Turbines with Grid Failure Detection Operating in Stand-Alone and Grid-Connected Mode. *IEEE Trans. Power Electron.*, 19(5), 1323-1332.

[45] Wang, Q., & Chang, L.-C. (2004). An Intelligent Maximum Power Extraction Algorithm for Inverter-Based Variable Speed Wind Turbine Systems. *IEEE Transactions on Power Electronics*, 19(5), 1242-1249.

[46] Song, Y., Dhinakaran, B., & Bao, X. (2000). Variable Speed Control of Wind Turbines Using Nonlinear and Adaptive Algorithms. *Journal of Wind Engineering and Industrial Aerodynamics*, 85(3), 293-308.

[47] Chinchilla, M., Arnaltes, S., & Burgos, J.-C. (2006). Control of Permanent-Magnet Generators Applied to Variable-Speed Wind-Energy Systems Connected to the Grid. *IEEE Transactions on Energy Conversion*, 21(1), 130-135.

[48] Koutroulis, E., & Kalaitzakis, K. (2006). Design of a Maximum Power Tracking System for Wind-Energy-Conversion Applications. *IEEE Transactions on Industrial Electronics*, 53(2), 486-494.